

Diss. ETH No. 13668 and
ETHZ-IPP Internal Report 2000-04

Muon Pair Production with high Invariant Mass in e^+p – Collisions at HERA

A dissertation submitted to the
Swiss Federal Institute of Technology Zurich
for the degree of
Doctor of Natural Sciences

presented by
Hans-Christian Kästli

dipl. phys. ETH
born November 14th, 1970
citizen of Luzern / GR

accepted on the recommendation of
Prof. Dr. Ralph A. Eichler, examiner and
Prof. Dr. André Rubbia, co-examiner

April 2000

Abstract

Many processes in physics beyond the standard model show the signature of isolated leptons. A possible excess of events with one isolated lepton and high missing transverse energy was reported in 1998 by the H1 collaboration.

Possible explanations are statistical fluctuations, detector effects or new physics beyond the standard model. The last two explanations could also be visible in the channel with two isolated leptons.

This analysis measures the cross section for the production of two isolated muons in the elastic and inelastic channel in the kinematic range $20^\circ < \theta^\mu < 160^\circ$, $M^{\mu\mu} > 5 \text{ GeV}/c^2$ and $p_T^\mu > 1.8 \text{ GeV}/c$. The data were collected during the years 1996 and 1997, which corresponds to an integrated luminosity of $32.4 \pm 0.9 \text{ pb}^{-1}$. The result is

$$\begin{aligned}\sigma_{vis}^{el}(e^+p \rightarrow \mu^+\mu^-X) &= (26.6 \pm 2.2 \pm 2.9) \text{ pb} \\ \sigma_{vis}^{in}(e^+p \rightarrow \mu^+\mu^-X) &= (20.2 \pm 2.4 \pm 3.6) \text{ pb}\end{aligned}$$

which is in good agreement with the expectation from the standard model. Also the differential distributions with respect to P_T^X , P_T^{miss} and $M^{\mu\mu}$ agree with the expectation.

No signal for new physics has been found.

Zusammenfassung

Viele Prozesse in der Physik ausserhalb des Standardmodells zeigen eine Signatur mit isolierten Leptonen. Ein möglicher Überschuss von Ereignissen mit einem isolierten Lepton und hohem fehlenden Transversalimpuls wurde 1998 durch die H1 Kollaboration publiziert.

Mögliche Erklärungen sind statistische Fluktuationen, Detektoreffekte oder neue Physik ausserhalb des Standardmodells. Die zwei letzteren könnten auch im Kanal mit zwei isolierten Leptonen sichtbar sein.

Diese Analyse misst den Wirkungsquerschnitt für die Produktion von zwei isolierten Muonen im elastischen und inelastischen Kanal im kinematischen Bereich von $20^\circ < \theta^\mu < 160^\circ$, $M^{\mu\mu} > 5 \text{ GeV}/c^2$ und $p_T^\mu > 1.8 \text{ GeV}/c$. Die Daten wurden in den Jahren 1996 und 1997 aufgezeichnet, was einer integrierten Luminosität von $32.4 \pm 0.9 \text{ pb}^{-1}$ entspricht. Das Resultat ist

$$\begin{aligned}\sigma_{vis}^{el}(e^+p \rightarrow \mu^+\mu^-X) &= (26.6 \pm 2.2 \pm 2.9) \text{ pb} \\ \sigma_{vis}^{in}(e^+p \rightarrow \mu^+\mu^-X) &= (20.2 \pm 2.4 \pm 3.6) \text{ pb}\end{aligned}$$

was in guter Übereinstimmung mit der Erwartung aus dem Standardmodell ist. Auch die differentiellen Verteilungen bezüglich P_T^X , P_T^{miss} und $M^{\mu\mu}$ stimmen mit den Erwartungen überein.

Kein Anzeichen für neue Physik wurde gefunden.

Contents

1	Motivation	4
1.1	The Search for Physics beyond the Standard Model	4
1.2	Events with an Isolated High Energy Lepton	5
2	Muon - Pair Production in QED	12
2.1	Production Processes	12
2.2	Monte Carlo	12
2.2.1	Inclusion of Compton like Graphs	15
2.2.1.1	Helicity Method	16
2.2.1.2	Comparison with 2-Photon Generator	19
2.2.2	The Representation of the Proton	19
2.2.2.1	Elastic Scattering	21
2.2.2.1	Inelastic Scattering	21
2.2.2.3	Deep Inelastic Scattering	22
2.2.3	Distribution of Generated Variables	22
3	Experimental Setup	25
3.1	The HERA Collider	25
3.2	The H1 Detector	26
3.2.1	The Tracking Systems	29
3.2.2	The Calorimeters	31
3.2.3	The Muon Systems	32
3.2.4	The Trigger System	34
3.2.4.1	Definition of Subtrigger 34	35
3.2.4.2	Definition of Subtrigger 15	36
3.2.4.2	Definition of Subtrigger 87	37
4	Data Selection	39
4.1	Track Selection	39
4.2	Energy Measurement	41
4.3	Muon Identification	41
4.3.1	Muon Reconstruction in the Instrumented Iron	42
4.3.2	Muon Reconstruction in the LAr Calorimeter	44
4.4	Event Selection	46

4.5	Selection Efficiency	47
4.6	Trigger Efficiencies	50
4.6.1	Trigger Efficiencies on Level 1	50
4.6.2	Trigger Efficiencies on Level 2 and 4	51
4.7	Luminosity	54
4.8	Picture of Typical Events	57
5	Measurement of the Cross Section	59
5.1	Background	59
5.2	Definition of Elastic and Inelastic Cross Section	62
5.3	Systematic Errors	66
5.3.1	Monte Carlo	66
5.3.2	Data	67
5.4	Results	68
5.5	Differential Distributions	69
5.6	Relaxed Muon Reconstruction Cuts	74
6	Multi Muon Events	76
	Conclusions	81
	Acknowledgements	86
	Curriculum vitae	87

Chapter 1

Motivation

1.1 The Search for Physics beyond the Standard Model

The concept of *local gauge symmetry* has proven as one of the most fruitful concepts in modern particle physics. The so called *Standard Model (SM)* of particle physics consists of a local $SU(2)_L \otimes U(1)_Y$ symmetry for electroweak interaction (broken down to $U(1)_{em}$ electromagnetic interaction) and a $SU(3)_C$ gauge symmetry for strong interaction. Apart from some recent results in neutrino physics, no deviation from the *SM* has been observed until now.

However, from a theoretical point of view, the *SM* can hardly be the end of physics. A “*good*” theory should explain the huge number of free parameters in the *SM* (at least 19), especially the particle masses (which one would expect to be at the Planck scale), the origin of the six flavours of quarks and leptons and their weak charged current mixing and CP violation. Also it is tempting to try to unify all the particle interactions in a simple gauge group.

For this reason, theoretical physicists are looking for theories beyond the standard model, from which the later appears naturally as a low energy limit. The most popular extensions are the Supersymmetric Theories. Many of these theories predict new phenomenology at an energy scale close to the center of mass energy of today's particle colliders. Therefore, one is looking with great effort for new resonances or new event signatures. So far, searches for supersymmetric particles have led only to exclusion limits in parameter spaces. However, there are observations of very few events, which are not fully understood. It is the measurement of an event with the signature $p\bar{p} \rightarrow \gamma\gamma ee +$ high missing transverse momentum at CDF [3] and the observation of a possible excess of events with an isolated lepton and missing transverse momentum at the H1 detector [4]. These events could give a hint on new physics, although they have not much predictive power, because of the very poor statistic.

The significance of these measurements strongly depends on the knowledge of the background. Looking at the H1 measurement, one of the main background sources

is the QED production of muon pairs where one muon escapes the detector unseen. In the next section we will focus a little bit closer on the isolated lepton measurement. We will see how this motivates the study of lepton pair production with high invariant mass, which is done in this analysis.

1.2 Observation of Events with an Isolated High Energy Lepton and Missing Transverse Momentum at HERA

As reported in [4] a search for events with an isolated high energy lepton and an imbalance in transverse momentum has been performed with the H1 detector at HERA. A very short overview is given here.

The data was collected between 1994 and 1997, corresponding to an integrated luminosity of $41 \pm 1 \text{ pb}^{-1}$. In this thesis the ep running period from 1999 has been added which corresponds to an integrated luminosity of another $16 \pm 1 \text{ pb}^{-1}$. The selection criteria are

- $p_T^{calo} > 25 \text{ GeV}/c$ (20 GeV/c for muon production in 1999). p_T^{calo} is the vector sum of the energy deposited in the central calorimeters.
- There is at least 1 track with $p_T > 10 \text{ GeV}/c$ and $\theta > 10^\circ$, where p_T is the transverse momentum as measured by the tracker and θ is the polar angle.
- A reconstructed vertex has to be found in the ep interaction region, and a set of topological and timing requirements are applied, in order to reject non- ep events.
- to reject NC events with energy lost in calorimeter cracks or in the beam pipe, events are rejected if there is an identified scattered positron and one of the following conditions is fulfilled:
 - the momentum from the positron is balanced by the hadronic system in azimuth within $\Delta\Phi = 5^\circ$. The scattered quark and the scattered positron are moving back to back.
 - $\delta := \sum_i E_i(1 - \cos \theta_i) > 45 \text{ GeV}/c$, where E_i and θ_i denote the energy and polar angle of the particles in the final state. For events with the scattered positron in the detector, δ peaks at twice the initial positron energy, that is, at 54 GeV/c.

In the remaining sample the isolation of the high p_t tracks was studied. The used observables were

- D_{jet} , their distance to the closest hadron jet in the pseudorapidity - azimuth plane: $D_{jet} = \sqrt{\Delta\eta^2 + \Delta\phi^2}$
- D_{track} , their distance in $\eta - \phi$ to the closest track

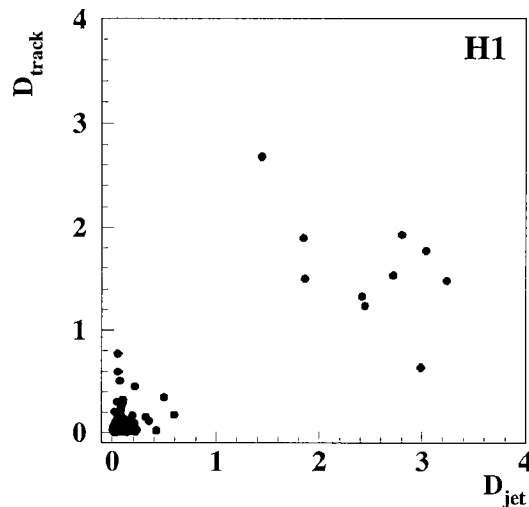


Figure 1.1: Distance to the closest hadronic jet (D_{jet}) and to the closest track (D_{track}) for all high p_T tracks in the sample

The bulk of events with an intrinsic imbalance of transverse momentum comes from charged current (CC) interactions. There, an isolated muon can only originate from heavy quark or π/K decays. Thus, one would expect, that the high- p_T tracks are not clearly isolated. Figure 1.1 shows the measurement. Indeed, in most cases the tracks are not isolated. But 10 events have the signature of **one** high- p_T track which is well separated from all other activities in the detector.

In 3 events this track is assigned to an electron candidate, while the other 7 events are assigned to an isolated muon. The production of this type of events has been studied within the standard model. In table 1.1 the observed and predicted rates are shown for the electron and the muon channel. The dominating contributions are W production ($ep \rightarrow el\nu_l X$, $ep \rightarrow \nu_e l\nu_l X$) and QED lepton pair production ($ep \rightarrow el^+l^- X$) where one of the two leptons escapes the detector undetected.

Other contributions come from neutral current ($ep \rightarrow eX$) and charged current ($ep \rightarrow \nu_e X$) interactions, where the lepton is a misidentified hadron, heavy quark production with subsequent semileptonic decays, Z production ($ep \rightarrow eZX$, $Z \rightarrow l^+l^-$) where one lepton escapes the detector unseen and photo production of two

	muons	electrons
Data	7	3
W Production	0.83 ± 0.17	2.34 ± 0.67
Z Production	0.01 ± 0.01	0.01 ± 0.01
Charged Current interaction (CC)	0.01 ± 0.01	0.03 ± 0.02
Neutral current interaction (NC)	0.18 ± 0.12	0.75 ± 0.14
Photoproduction	< 0.03	< 0.03
Heavy Quarks	< 0.06	< 0.05
Lepton Pair Production in QED	0.28 ± 0.07 ¹	0.19 ± 0.06
all MC	1.40 ± 0.22	3.40 ± 0.69

Table 1.1: Observed and predicted event rates. The numbers refer to the summed production of positive and negative leptons. The limits correspond to 95% confidence level. In the muon channel the main sources are W production and lepton pair production. The asymmetry between electron and muon channel is due to the cut on p_T^{calo} . In the muon channel, it acts more or less as a p_T^X cut.

jets, where one fluctuates into a single hadron which is misidentified as a lepton.

The observed rate in the muon channel is roughly a factor of 5 higher than what is expected from Monte Carlo simulations. The probability to see at least 7 muons with an expectation of 1.40 ± 0.22 events is calculated as

$$\mathcal{P}(N \geq 7) = \int_0^\infty dx G(x; 1.40, 0.22) \sum_{k=7}^\infty p(k; x),$$

where

- $G(x; 1.40, 0.22)$ is the probability density function for the expectation value. It is a Gaussian with mean 1.40 and width 0.22.
- $p(k; x)$ is the Poisson probability to observe k events with an expectation of x events.

The result is $\mathcal{P}(N \geq 7) = 8.4 \cdot 10^{-4}$.

Figures 1.2 and 1.3 show the distributions of the hadronic transverse momentum P_T^X , (which is the transverse part of the vector sum of the energy deposited in the LAr and tail catcher calorimeter not assigned to a lepton) and the missing transverse momentum p_T^{miss} in the muon channel. There is not only a mismatch in the normalization, but also a tendency to higher values of p_T^X in the data.

Figures 1.4 and 1.5 show the same distributions in the electron channel. The normalizations are in good agreement, while the shape again tends to higher p_T^X in the data.

¹The error as stated in the H1 paper is substantially higher. Due to low statistics for tests of the LPAIR generator, the inelastic contribution was conservatively allowed to vary within a factor of 2. Due to the present analysis, this error could be lowered.

Possible explanations for an excess of events could be:

1. It is just a statistical fluctuation. As stated before the probability for this to occur is very small.
2. The long tail in the P_T^X distribution in the data could be a detector effect.
3. There are models beyond the standard model, which produce events with the signature of isolated muons:
 - According to [5], three of the muon events are compatible with the hypothesis of production of excited quarks ($q^* \rightarrow qW \rightarrow q\mu\nu_\mu$) within compositeness models.
 - In Rp violating SUSY, this signature may occur in the decay of a squark $\tilde{u}_L \rightarrow d\chi_1^+$ and the subsequent gauge decay $\chi_1^+ \rightarrow W^+\chi_1^0 \rightarrow l^+\nu\chi_1^0$ (see decay channel S6 in [6]).

From this, the following questions arise:

1. How good is the measurement of muons in H1? Is the tail at high P_T^X a detector effect? Misidentified leptons could add a substantial imbalance in hadronic energies.
2. Is the description of the background in the Monte Carlo simulation correct? Of special interest here is the distribution of p_T^X and p_T^{miss} .
3. If W 's are produced from excited quarks, there should also be Z^0 production. Is this seen?
4. In the Rp-violating scenario, the down type quark could be a b quark decaying into $c\mu\nu$. This would add to the channel with two isolated muons and high missing energy. Are there any such events?

Muon pair production in EW theory is a dedicated process to answer the first two questions because

1. The cross section is well known. There are few theoretical uncertainties because of higher order corrections and the background is very low. This predestines it to check the measurement of muons.
2. If the tails in the P_T^X distributions are detector effects, this would also be visible in the two muon channel. Thus, we have a possibility to investigate and eventually exclude this effect.

3. the Monte Carlo generator for this process is the least tested generator at these energies. It contains only two photon physics. The question has to be answered, whether other graphs contribute substantially at higher energies. Since QED is one of the main background sources, this could alter the distributions in figure 1.2 and 1.3. A previous analysis about muon pair production ([20]) leaves room for this, since a mismatch in the total cross section of about 60% has been found.

The following analysis investigates exactly these questions. In chapter 2 this is done on generator level. The influence of other processes is analyzed. In chapter 3 a description of the detector follows. The measurement of muons is investigated extensively in chapter 4. In chapter 5 the muon production cross section is determined. Finally, events with three muons have been found. Since multi muon events are very rare, some of the muons should be misidentified hadrons. This is analyzed in chapter 6.

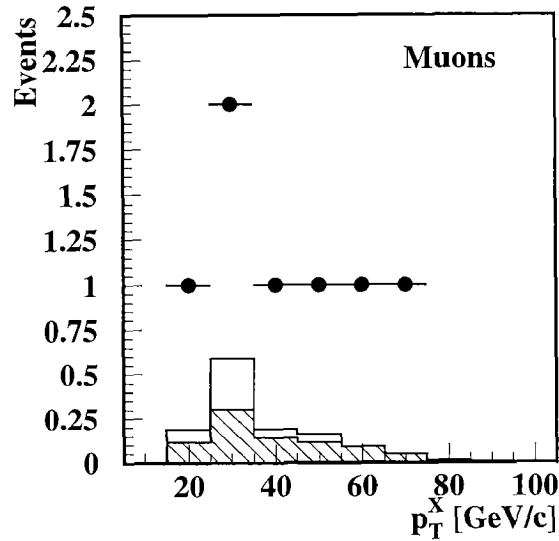


Figure 1.2: Differential distribution of p_T^X for isolated muon production. Dots represent data, the dashed histogram shows W production and the open histogram shows NC and two photon events added to it. Aside from the normalization there is a tendency to higher values in the data.

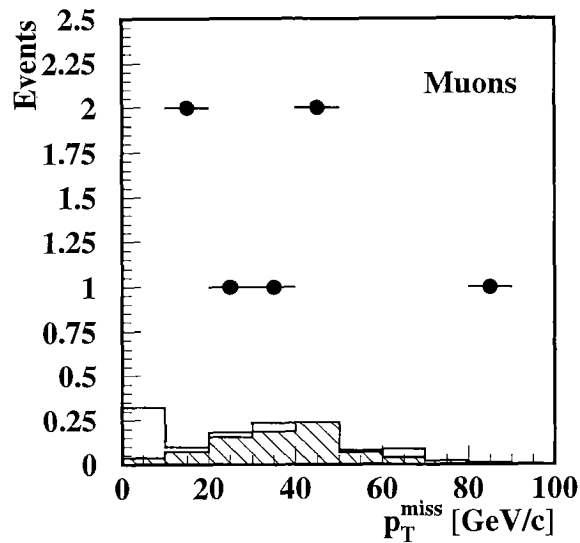


Figure 1.3: Differential distribution of p_T^{miss} for isolated muon production. Dots represent data, the dashed histogram shows W production and the open histogram shows NC, two photon events and W production.

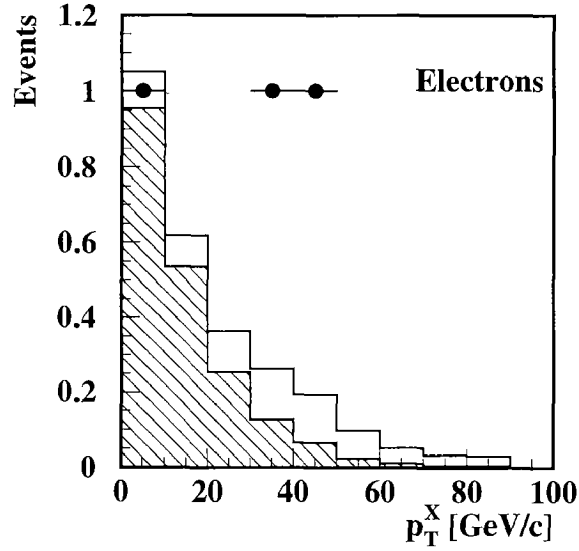


Figure 1.4: Differential distribution of p_T^X for isolated electron production. Dots represent data, the dashed histogram shows W production and the open histogram shows NC and two photon events added to it. The integral above $p_T^X=20$ GeV/c in Monte Carlo is 0.29 events compared to 2 events in data.

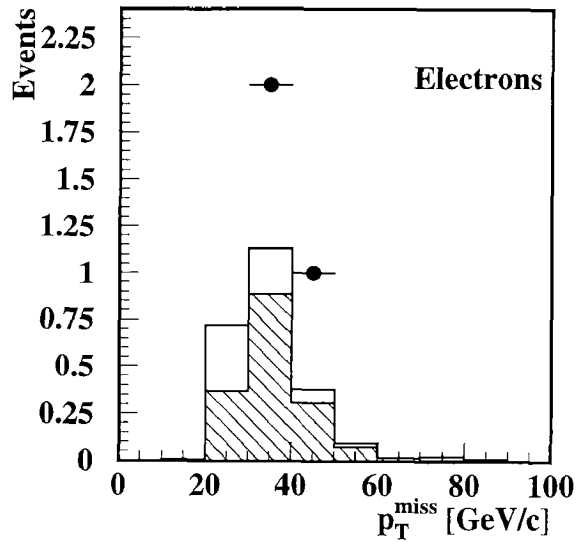


Figure 1.5: Differential distribution of p_T^{miss} for isolated electron production. Dots represent data, the dashed histogram shows W production and the open histogram shows the sum of W production NC and two photon events.

Chapter 2

Muon - Pair Production in QED

2.1 Production Processes

This chapter describes the production of muon pairs on generator level. So far, in H1 the generator LPAIR has been used for this process. It is based on the work of J.A.M. Vermaseren [22] and includes only two photon physics (so called Bethe-Heitler process). This is the dominating contribution to muon pair production in QED.

In figure 2.1 other non-resonant processes are shown. The relative weight of these graphs have been investigated in [21] as a function of the transverse momentum p_T of one of the two muons. Figure 2.2 is taken from there and shows the various contributions to $p_T^3 \frac{d\sigma}{dp_T}$ as a function of the transverse momentum p_T of one of the two generated leptons.

The differential cross section for direct and resolved ¹ Drell-Yan processes (figure 2.1 e,f) is about two orders of magnitude smaller than for the two photon graphs up to $p_T=25$ GeV/c. Then it rises but stays an order of magnitude smaller at $p_T = 40$ GeV/c. They are neglected in the following.

For $p_T < 20$ GeV/c the contribution of the Compton like processes (figure 2.1 c,d) is smaller than 1% but reaches the same order of magnitude at 40 GeV/c. In a previous analysis ([20]) the measurement of the muon pair production cross section was about 60% higher than expected. It was supposed that it could be the influence of these graphs. This question is answered in the following.

2.2 Monte Carlo

At the time of the beginning of this analysis the only available Monte Carlo generator for lepton pair production in ep colliders was LPAIR. This will be extended

¹*direct* means the pointlike interaction with the photon, while *resolved* means the interaction with a quark within the photon structure

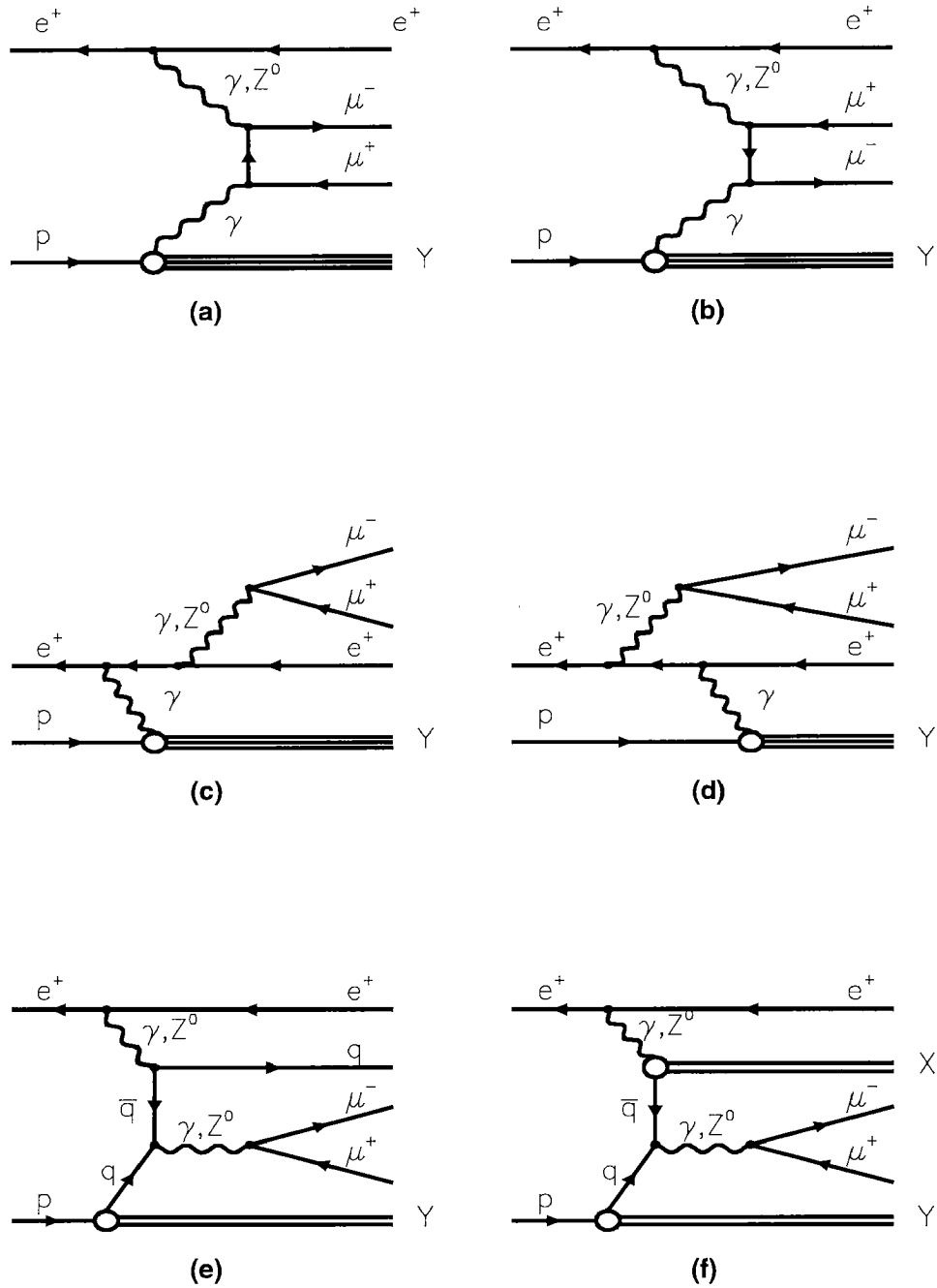


Figure 2.1: Feynman graphs for different production processes: Bethe-Heitler process (a) and (b), Compton like processes (c) and (d), Drell-Yan direct (e) and resolved (f).

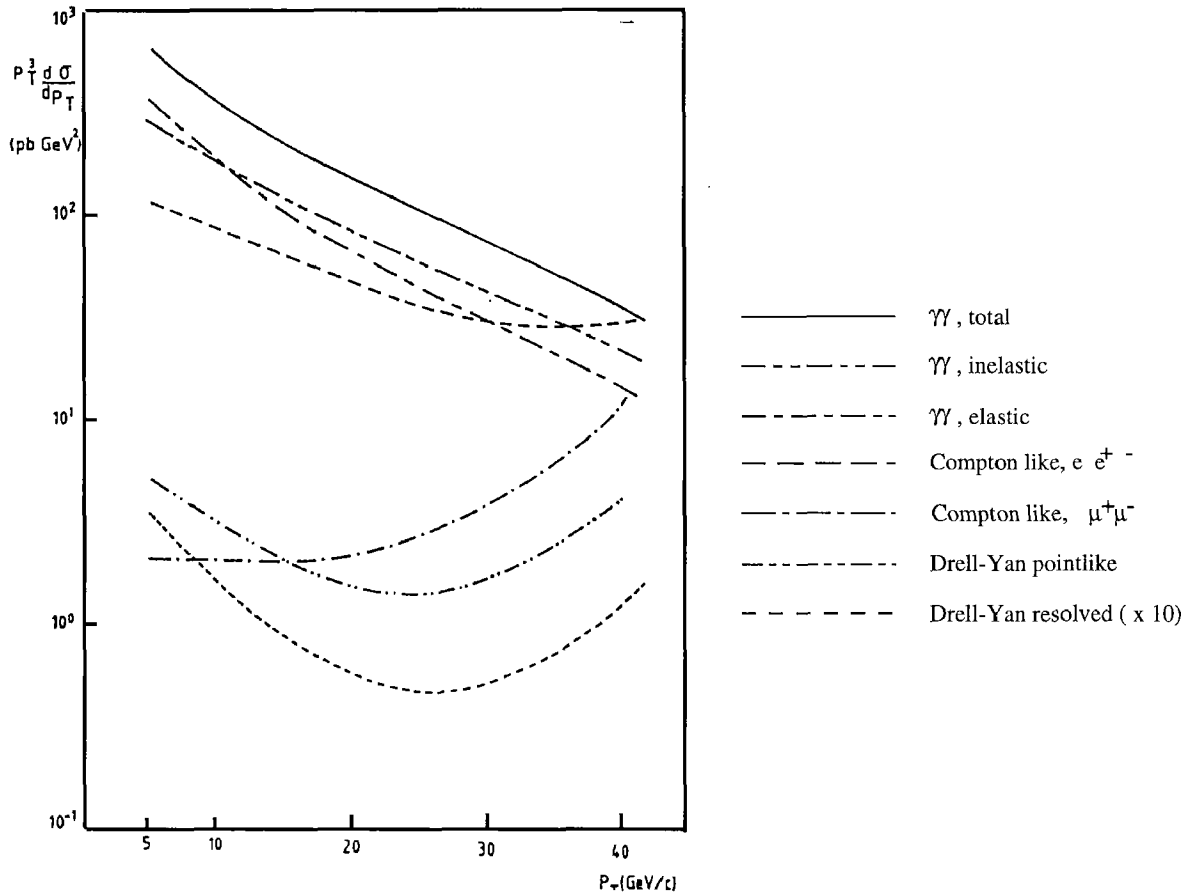


Figure 2.2: Various contributions to $p_T^3 \frac{d\sigma}{dp_T}$ for lepton pair production as a function of the transverse momentum of one of the two leptons.

here. In a first step the matrix element has been rewritten. In the following this generator is called LPAIR++. Since in the muon channel the Compton like graphs did not add a severe peaking behaviour of the matrix element no new phase space generator has been developed.

In the meantime an independent generator GRAPE ([31]) is available. The extended generator LPAIR++ has been cross checked with GRAPE. The result has been used to estimate a systematical error in the expectation and can be found in chapter 5.

Apart from Drell-Yan processes, the event structure for muon pair production looks like in figure 2.3. There are two systems in the final state. The system X is the part which was altered in LPAIR++. A short description of how this is done is given in section 2.2.1.

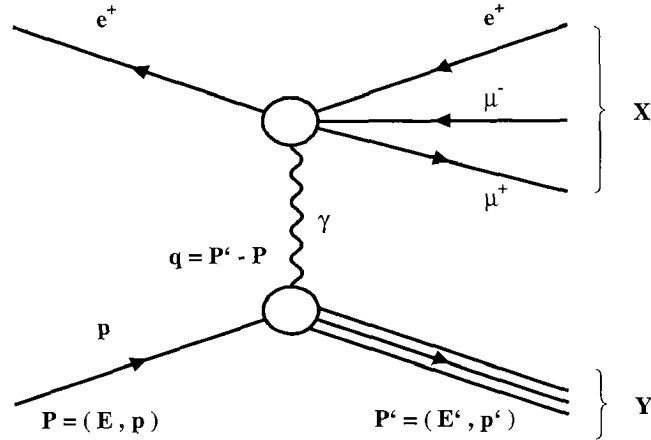


Figure 2.3: Schematics of an event in muon pair production.

The system Y describes the final state of the scattered proton. In case of elastic scattering ² the system Y consists only of a proton. This is dominant for low Q^2 , which is defined as $Q^2 = -q^2$ and $q = P' - P$ is the four momentum transferred to the proton. For inelastic scattering two modes exist in LPAIR, which distinguish the resonance region at low Q^2 and mass M_Y of the system Y and the DIS (deep inelastic scattering) region at high Q^2 . The description of this hadronic part is unaltered from LPAIR and is described in section 2.2.2.

2.2.1 Inclusion of Compton like Graphs

A new matrix element has to be written, which includes the graphs 2.1 (a) to (d) including the exchange of a Z^0 . Although it is a leading order calculation it is non-trivial for two reasons.

1. The standard method, involving squaring the amplitude and summing over spin states, produces a large multiplicity of terms
2. there is very strong numerical cancelation between various terms. This can be so bad, that even double precision calculation would not suffice [22]

²Note, that *elastic* scattering here does not mean, that there is only a proton and an electron in the final state, but that the system Y is a proton.

A method which addresses both items, is the *Helicity Method* [1]. This is briefly described in the following without going into much technical details. Also the proofs can be found in [1] and are not repeated here.

2.2.1.1 Helicity Method

The trick is to compute \mathcal{M} instead of $\sum |\mathcal{M}|^2$, where \mathcal{M} is the matrix element, and the sum goes over external spins. This addresses point 2 above, since the cancellations will take place over less orders of magnitude.

It is not possible to express \mathcal{M} in terms of scalar products of external momenta $p_i \cdot p_j$. Instead, we need something which is proportional to the square root of it. These are the spinor products $\bar{u}(p_j)u(p_j)$ which we are going to develop in the next subsections. From a computational point of view, we must find a representation where they are not much more complicated to evaluate than scalar products.

Massless Spinors

Because we will reduce the case of massive fermions to the case of massless fermions, we will start with the later.

For a spinor with lightlike momentum p and helicity λ we have

$$u_\lambda(p)\bar{u}_\lambda(p) = P_\lambda \not{p} \quad (2.1)$$

where $P_\lambda = \frac{1}{2}(1 + \lambda\gamma^5)$ is the projection operator onto states with helicity λ . Now, we choose two four-vectors k_0^μ and k_1^μ with the properties

$$k_0 \cdot k_0 = 0, \quad k_1 \cdot k_1 = -1, \quad k_0 \cdot k_1 = 0. \quad (2.2)$$

Then we define (up to its complex phase) a basic spinor with negative helicity through

$$u_-(k_0)\bar{u}_-(k_0) = P_- \not{k}_0 \quad (2.3)$$

and a positive helicity state through

$$u_+(k_0) = \not{k}_1 u_-(k_0) \quad (2.4)$$

which satisfies (2.1) because of (2.2).

For any lightlike momentum p we can define the corresponding spinors through

$$u_\lambda(p) = \frac{1}{\sqrt{2p \cdot k_0}} \not{p} u_{-\lambda}(k_0) \quad (2.5)$$

which again satisfy (2.1). The only restriction is, that the denominator has to be nonzero.

One can find expressions for the spinor products

$$s(p_i, p_j) \equiv \bar{u}_+(p_i)u_-(p_j) = -s(p_j, p_i) \quad (2.6)$$

$$t(p_i, p_j) \equiv \bar{u}_-(p_i)u_+(p_j) = s^*(p_j, p_i) \quad (2.7)$$

which are quite compact if we choose

$$k_0^\mu = (1, 1, 0, 0) \quad (2.8)$$

$$k_1^\mu = (0, 0, 1, 0) \quad (2.9)$$

$$p_i^\mu = (p_i^0, p_i^x, p_i^y, p_i^z) \quad (2.10)$$

namely

$$s(p_i, p_j) = (p_i^y + ip_i^z) \left(\frac{p_j^0 - p_j^x}{p_i^0 - p_i^x} \right)^{1/2} - (p_i \leftrightarrow p_j) \quad (2.11)$$

The second term is the same as the first with the two momenta interchanged. Due to this explicit anti-symmetrization, the calculation is stable even if the two momenta become collinear.

Massive Spinors

For a fermion with momentum q and mass m , we need a spinorial object which leads to the correct spin sum which is

$$\sum_\lambda u(q, \lambda) \bar{u}(q, \lambda) = \not{q} \pm m \quad (2.12)$$

for fermions (+) and antifermions (-). Here, $\lambda = \pm$ is the sign of the projection of the spin onto some fixed vector s^μ . With some lightlike momentum k , a good spinor for a fermion is

$$u(q, +) = \frac{1}{\sqrt{2q \cdot k}} (\not{q} + m) u_-(k), \quad (2.13)$$

i.e. we can find a unique spin vector s^μ such that the Dirac equations hold. Next, we choose two lightlike momenta p_1 and p_2 which build up q and choose p_2 for k :

$$p_1^2 = p_2^2 = 0, \quad p_1^\mu + p_2^\mu = q^\mu, \quad p_2^\mu = k^\mu \quad (2.14)$$

For this choice, the spin vector gives

$$s^\mu = (p_1^\mu - p_2^\mu) / m \quad (2.15)$$

One gets the other spin state / spinors for anti-fermions by changing $u_-(k)$ into $u_+(k)$ / $+m$ into $-m$ in (2.13). The spinor products of massive fermions have the same structure as (2.11) but with the corresponding spacelike momenta.

The Matrix Element

The calculation of \mathcal{M} also solves problem 1 above, because the complexity grows only linearly with the number of graphs. Moreover, the same computer code can be used for the different graphs with permutations of the external momenta. We do not give all the details but show the key point with the example of DIS, where we have lepton quark scattering. This follows closely ref. [2], where it is used in a $e^+e^- \rightarrow e^+e^-l^+l^-$ generator.

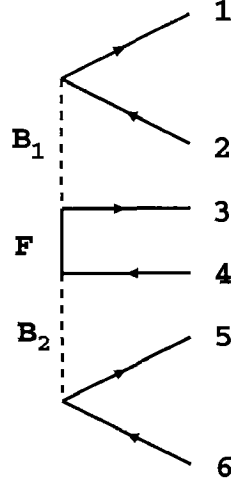


Figure 2.4: Generic graph for muon production in DIS.

Figure 2.4 shows the generic graph. Solid lines are fermions and dashed lines are bosons (photons or Z^0). All the feynman diagrams can be obtained by different assignments of the external momenta to the legs of the graph. For the propagators we can write

$$\begin{aligned}
 B_1 &= \frac{g^{\mu\nu}}{(b_1 p_1 + b_2 p_2)^2 - m_{B_1}^2 + im_{B_1} \Gamma_1} \\
 B_2 &= \frac{g^{\mu\nu}}{(b_5 p_5 + b_6 p_6)^2 - m_{B_2}^2 + im_{B_2} \Gamma_2} \\
 F &= \frac{Q}{(b_1 p_1 + b_2 p_2 + b_3 p_3)^2 - m_3^2}
 \end{aligned}$$

The factors b_i are +1 (-1) if i is an outgoing (incoming) particle, p_i , m_i are the momentum and mass assigned to leg i of the graph, m_{B_i} , Γ_i are the mass and width of the boson i (0 for γ 's). Q is the spinorial part of the lepton propagator. If the masses of anti-fermions are taken *negative*, it is

$$Q = b_1(\not{p}_1 + m_1) + b_2(\not{p}_2 + m_2) + b_3(\not{p}_3 + m_3)$$

If we write $u(q, s)$ for both, the fermionic and anti-fermionic spinors (the type shall be implied by the argument), the total spinorial part of \mathcal{M} is

$$S = \bar{u}(p_1, s_1) \Gamma_1^\mu u(p_2, s_2) \times \bar{u}(p_3, s_3) \Gamma_{2\mu} Q \Gamma_{3\nu} u(p_4, s_4) \times \bar{u}(p_5, s_5) \Gamma_4^\nu u(p_6, s_6)$$

where Γ_i are the vertex couplings:

$$\begin{aligned}
 \Gamma_i^\mu &= ie\gamma^\mu, & \text{for photon couplings} \\
 \Gamma_i^\mu &= \frac{-ig}{4 \cos \theta_W} \gamma^\mu (1 - \gamma^5), & \text{for } Z^0 \text{ couplings}
 \end{aligned}$$

Using the relation (2.12) this can be written in the form

$$S = \sum_{\lambda} \sum_{i=1}^3 b_i G(p_1, \lambda_1; \Gamma_1; p_2, \lambda_2; p_3, \lambda_3; \Gamma_2; p_i, \lambda) G(p_i, \lambda; \Gamma_3; p_4, \lambda_4; p_5, \lambda_5; \Gamma_6; p_6, \lambda_6)$$

with

$$G(p_1, \lambda_1; \Gamma_1; p_2, \lambda_2; p_3, \lambda_3; \Gamma_2; p_4, \lambda_4) = \bar{u}(p_1, \lambda_1) \Gamma_1^{\mu} u(p_2, \lambda_2) \bar{u}(p_3, \lambda_3) \Gamma_{2\mu} u(p_4, \lambda_4)$$

These functions can be expressed by spinor products as developed above. This is tabulated in [2] as a function of the spins.

2.2.1.2 Comparison with 2-Photon Generator

The new Monte Carlo generator LPAIR++ has been compared to the 2 photon generator LPAIR. If the new graphs are disabled in LPAIR++ the two generators are in agreement within statistical errors in all modes.

The effect of the Z^0 exchange can be seen in figure 2.5. However, the Z^0 peak corresponds to a cross section of 2.3 fb. With the corrected integrated luminosity of 17.8 pb^{-1} used in this work this corresponds to an expectation of 0.04 events and cannot be seen.

Figure 2.6 shows the same plot in the low invariant mass region. This plot has been made using the generator GRAPE which is available in the meantime and includes all electroweak graphs. A difference in the two generators is visible only in a mass range below $\approx 2 \text{ GeV}/c^2$. This is due to the Compton like processes (figure 2.1 (c) and (d) with photons). Furthermore, it is only visible in DIS where the momentum transferred to the proton is relatively high.

2.2.2 The Representation of the Proton

Three different modes are available to describe the vertex at the proton side..

1. Elastic scattering
2. Inelastic scattering in the kinematic range $Q^2 < 5 \text{ (GeV}/c)^2$
3. Deep inelastic scattering in the kinematic range $Q^2 > 5 \text{ (GeV}/c)^2$

Q^2 is the negative of the momentum transferred to the proton. The modes are described in the following. For a more detailed description see [23], [24], [25], [26], [27].

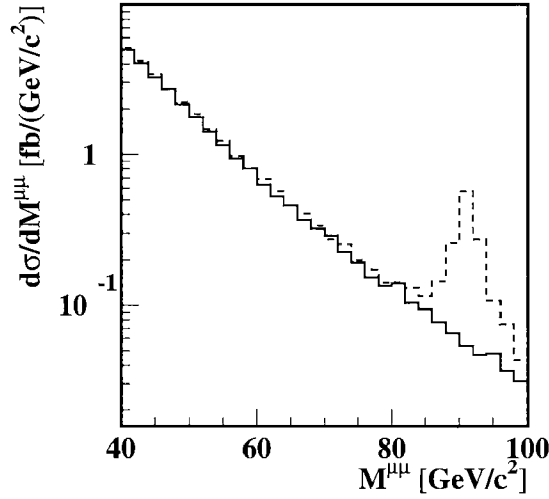


Figure 2.5: Cross section for μ pair production in the high invariant mass region in Monte Carlo simulation. The dashed histogram represents production with electroweak graphs included (LPAIR++), while the solid histogram represents the contribution from the two photon graphs only (LPAIR).

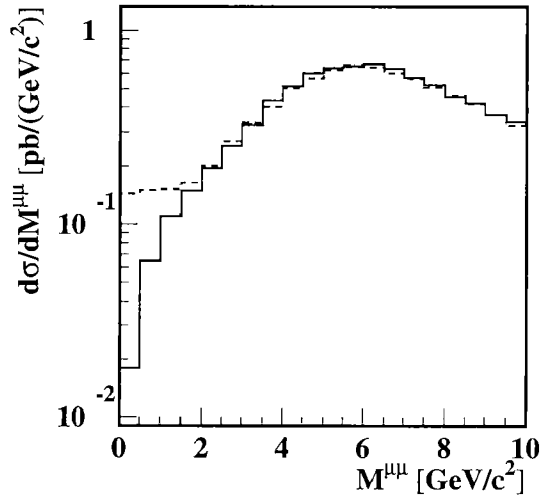


Figure 2.6: Cross section for μ pair production in the low invariant mass region in DIS Monte Carlo simulation. The dashed histogram represents production with Compton like graphs included (GRAPE), while the solid histogram represents the contribution from the two photon graphs only (LPAIR).

2.2.2.1 Elastic Scattering

The parametrization chosen here is

$$\frac{d\sigma_{el}}{d\Omega} = \frac{d\sigma}{d\Omega}\Big|_p \left[\frac{G_E^2(Q^2) + \tau G_M^2(Q^2)}{1 + \tau} + 2\tau G_M^2(Q^2) \tan^2 \frac{\Theta}{2} \right]$$

with

Θ the angle between the incoming positron and the outgoing leptonic system X ($e\mu\mu$) in the proton rest frame

$\frac{d\sigma}{d\Omega}\Big|_p$ the differential cross section of a pointlike fermion with the proton mass

$\tau = \frac{Q^2}{4m_P^2}$, where m_P is the proton mass

G_E and G_M the electric and magnetic form factors of the proton. They are approximated by the dipole factors.

$$G_E(Q^2) = \frac{G_M(Q^2)}{|\mu_P|} \approx G_D(Q^2) = \frac{1}{(1 + Q^2/0.71(\text{GeV}/c)^2)^2}$$

here μ_P is the magnetic moment of the proton.

2.2.2.2 Inelastic Scattering

The inelastic cross section can be written as

$$\frac{d^2\sigma_{in}}{dQ^2 d\nu} = \frac{4\pi\alpha^2}{Q^4} \cdot \frac{E'}{E} \cdot \left(W_2(Q^2, \nu) \cos^2 \frac{\Theta}{2} + 2W_1(Q^2, \nu) \sin^2 \frac{\Theta}{2} \right)$$

with

$$\nu = E - E'$$

E, E' are the energies of the incoming positron and the outgoing leptonic system X ($e\mu\mu$) in the rest frame of the proton

The structure functions W_1 and W_2 are parametrized in [26] and fitted to experimental data.

The resonance region, defined through $Q^2 < 6$ (GeV/c)² and $m_Y < 2$ GeV/c ², is parametrized separately in [27].

$$\sigma_{tot} = G_D^2 \exp \left[a(m_Y) + b(M_Y) \ln \frac{|\vec{q}|}{|\vec{q}_0|} + c(m_Y) \left(\left| \ln \frac{|\vec{q}|}{|\vec{q}_0|} \right| \right)^3 \right]$$

with

G_D the dipole form factor of the nucleon

$q = \begin{pmatrix} q_0 \\ \vec{q} \end{pmatrix}$ the 4-momentum transfered to the proton

Parameters a, b, c which depend only on the mass m_Y and are tabulated in ref. [27].

2.2.2.3 Deep Inelastic Scattering

The disadvantage of the inelastic mode is the fact that it doesn't supply a description of the hadronic final state. That's why another mode in the high Q^2 range was introduced, the DIS mode. In this mode the differential cross section for positron quark scattering is calculated and folded with the parton density function $f_{q/p}$ for the scattered quark according to

$$\frac{d\sigma_{ep}}{dQ^2} = \int \frac{d\sigma_{eq}}{dx dQ^2} \cdot f_{q/p}(x, Q^2) dx$$

The parton density function chosen here is CTEQ4 [28].

This description of the cross section is valid only in the high Q^2 regime. The cut value of 5 (GeV/c)² is justified by comparing the inelastic mode with the DIS mode as a function of Q^2 . The cut was made in a region where they coincide (see figure 2.7).

2.2.3 Distribution of Generated Variables

At the end of this chapter some distributions are presented. The events have been generated with the new generator LPAIR++. The following cuts have been used:

1. invariant mass: $M^{\mu\mu} > 4 \text{ GeV}/c^2$
2. polar angle: $10^\circ < \theta^\mu < 170^\circ$ for both muons
3. transverse momentum: $p_T^\mu > 1.0 \text{ GeV}/c$ for both muons
4. in the DIS mode: $Q^2 > 5 \text{ (GeV}/c)^2$

In figure 2.7 we see the generated distribution of $\log\left(\frac{Q^2}{\text{GeV}^2}\right)$. The open histogram shows events generated in the inelastic mode, the dashed histogram represents the

DIS mode. The absolute normalization is arbitrary but the relative normalization is correct. The cut has been made at $Q^2 = 5 \text{ (GeV/c)}^2$ indicated by the solid line. In the following '**inelastic mode**' always means the inelastic mode for $Q^2 < 5 \text{ (GeV/c)}^2$ and the DIS mode for $Q^2 > 5 \text{ (GeV/c)}^2$.

Figure 2.8 shows the distributions of the polar angles θ^μ , the transverse momentum p_T^μ and the invariant mass $M^{\mu\mu}$ of the generated muon pair and the opening angle $\theta^{\mu\mu}$ in three dimensions.

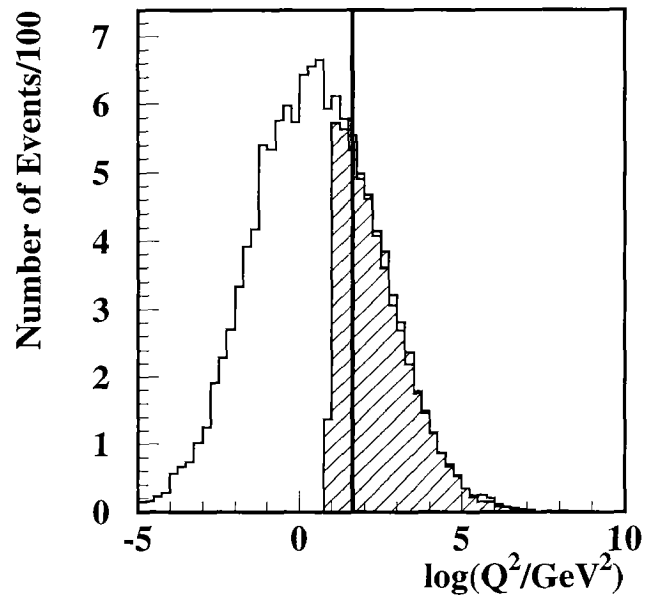


Figure 2.7: Distribution of $\log\left(\frac{Q^2}{\text{GeV}^2}\right)$. The open histogram represents the inelastic mode, the dashed histogram the DIS mode. The solid line indicates the cut used to separate the two modes.

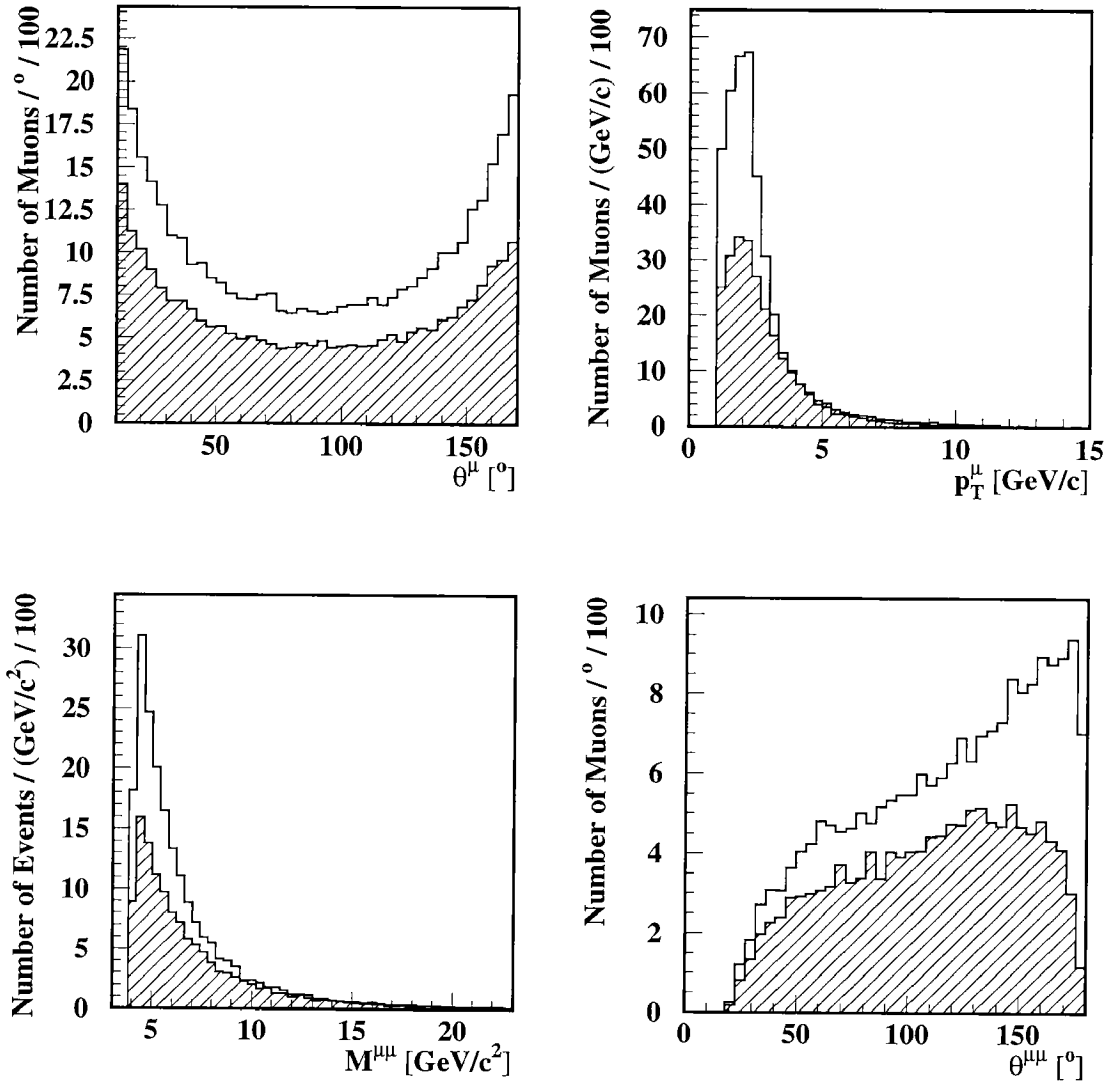


Figure 2.8: Distribution of polar angle and transverse momentum of the muons, invariant mass and opening angle of the two muons. The open histogram shows elastic, the dashed one inelastic muon production. The events are generated with LPAIR++ with the cuts: $M^{\mu\mu} > 4 \text{ GeV}/c^2$, $p_T^\mu > 1.0 \text{ GeV}/c$, $10^\circ < \theta^\mu < 170^\circ$.

Chapter 3

Experimental Setup

3.1 The HERA Collider

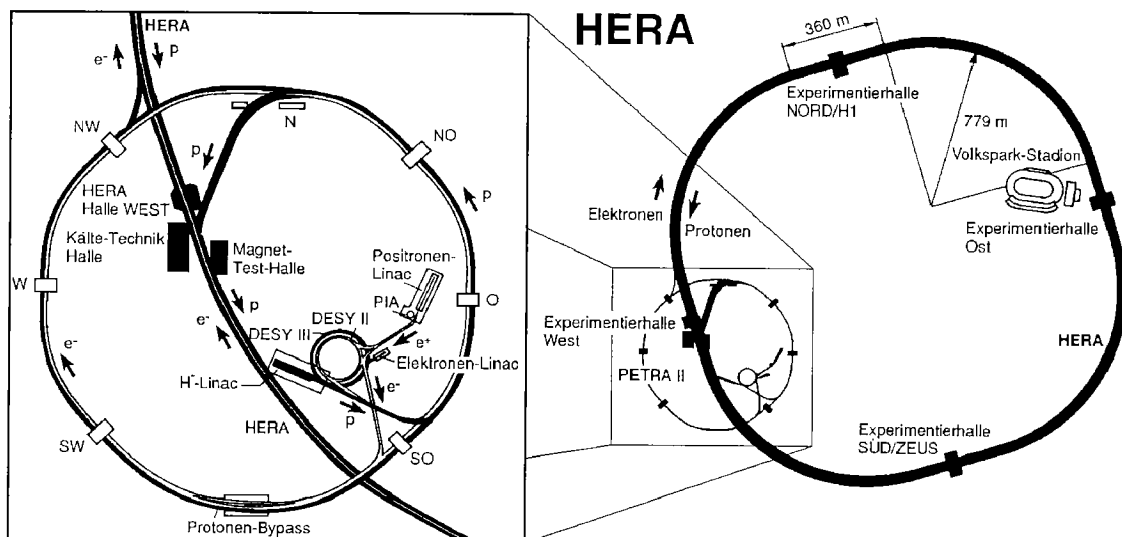


Figure 3.1: The accelerators at DESY

HERA (**H**adron **E**lectron **R**ing **A**nlage) is the first storage ring where electrons (here, electrons refers to both charge states, electrons and positrons) are brought to collision head on with protons. It is situated at the DESY laboratory in Hamburg and is in operation since 1992. Figure 3.1 shows a sketch of the ring and its preaccelerators. Protons and electrons are accelerated in Linac, DESY and PETRA up to an energy of 40 GeV and 14 GeV respectively. Then they are injected into HERA, where they are further accelerated to the final energy of 820 GeV and 27.5 GeV respectively. This corresponds to a center of mass energy of 300 GeV. Table 3.1 summarizes some parameters of the HERA collider.

Design parameter				
	p		e	
Circumference	6336 m			
CMS energy	300 GeV			
Luminosity	$1.5 \cdot 10^{31} \text{ cm}^{-2}\text{s}^{-1}$			
Bunch length σ_z	85 mm		9 mm	
Beam width σ_x, σ_y	0.3 mm, 0.05 mm		0.3 mm, 0.05 mm	
Energy loss per turn	6.2 eV		127 MeV	
96/97 running periods				
	1996		1997	
	p	e^+	p	e^+
Energy	821.6 GeV	27.6 GeV	821.1 GeV	27.5 GeV
Av. initial currents	65 mA	32 mA	77 mA	36 mA
Peak Luminosity	$8.3 \cdot 10^{30} \text{ cm}^{-2}\text{s}^{-1}$		$8.4 \cdot 10^{30} \text{ cm}^{-2}\text{s}^{-1}$	

Table 3.1: Some HERA collider parameters

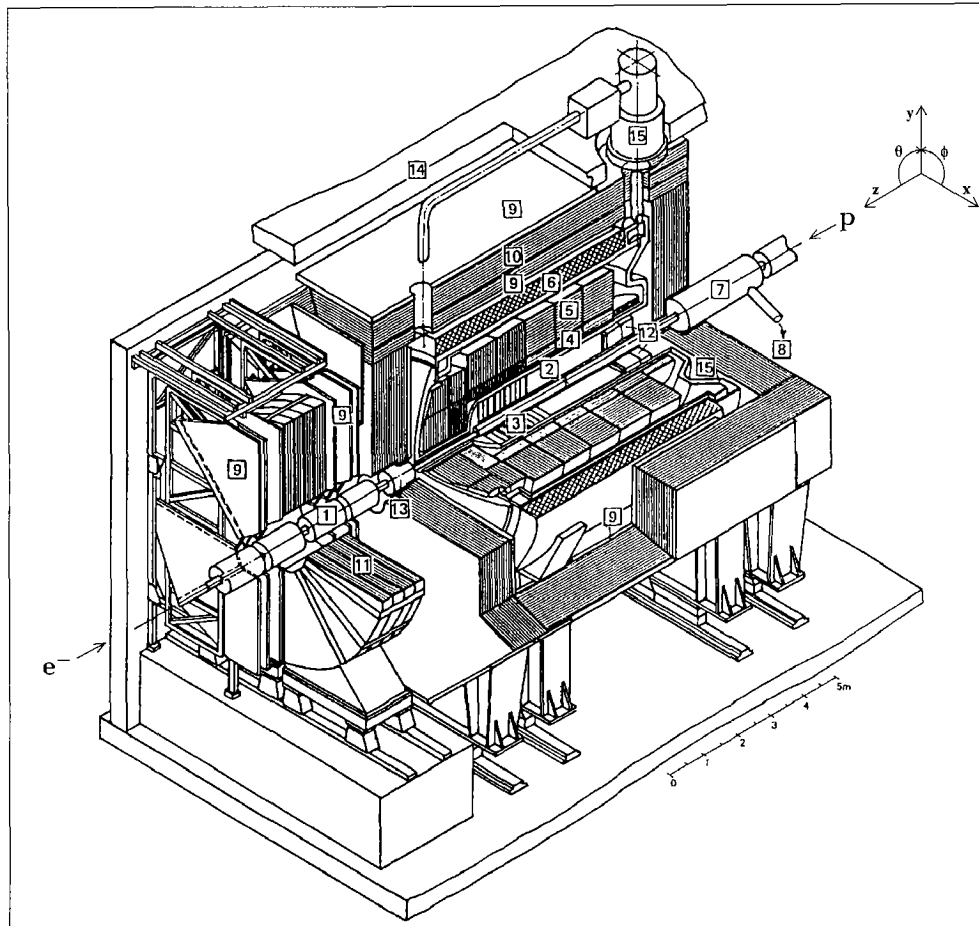
At two points along its circumference of 6336 m, the two beams are brought to collision. Two general purpose detectors (H1 and ZEUS) are built around these beam crossing points. Up to 210 bunches of protons and electrons can be stored. This leads to a frequency of bunch crossings of 10.4 MHz or a time interval between two bunch crossings of 96 ns.

Two more experiments are situated at HERA. HERMES uses the lepton beam only. It is investigating the spin structure of the proton. The other experiment, HERA-B, uses the proton beam only. It wants to measure CP violation in B meson decays and will soon start taking data.

3.2 The H1 Detector

Figure 3.2 shows a sectional drawing of the H1 detector [7] together with the H1 coordinate system. The origin of the coordinate system is in the nominal interaction point. The positive z-axis points in the direction of the proton beam and is referred to as *forward* direction. Accordingly, the *backward* direction is the direction of the lepton beam. As indicated in the figure, the polar and azimuthal angles θ and ϕ are defined relative to the forward direction and the x-axis respectively.

The detector is much more massive and more elaborately instrumented in the forward direction. This is necessary, because the $e-p$ center of mass system is boosted along the forward direction with $\gamma = \frac{1}{\sqrt{1-(v/c)^2}} = 2.86$.



1	Beam pipe and beam magnets	9	Muon chambers
2	Central tracking device	10	Instrumented iron yoke
3	Forward tracking device	11	Forward muon toroid
4	Electromagnetic LAr calorimeter	12	Spaghetti Calorimeter (SPACAL)
5	Hadronic LAr calorimeter	13	PLUG calorimeter
6	Superconducting coil (1.15 T)	14	Concrete shielding
7	Compensating magnet	15	Liquid argon cryostat
8	Helium supply for 7		

Figure 3.2: The H1 detector

From inside out, the main detector components are:

- Silicon vertex detector (not visible in the figure), consisting of two independent devices: the central silicon detector (CST) [8], and the backward silicon detector (BST). With this device it is possible to detect secondary vertices and the measurement of some track parameters can be improved.
- Central tracking device (2) and forward tracking device (3). They measure tracks from charged particles in the central and forward direction. The geometry of the tracks is the most important ingredient to reconstruct the kinematics. On the other hand, for low energetic particles, the trackers allow to identify the particle types by measuring the specific ionization loss.
- Liquid argon (LAr) calorimeter (4,5). There is an electromagnetic and a hadronic part. They are measuring the deposited energies and the extent and form of showers initiated by high energetic particles coming from the interaction region. It allows to distinguish efficiently between showers initiated by electrons/photons or hadrons.
- Spaghetti type calorimeter, Spacal (12). This is a calorimeter positioned in the backward region, designed to detect the scattered beam lepton. It consists of an electromagnetic and a hadronic section.
- Superconducting coil (6). It creates an almost homogeneous magnetic field of 1.4 Tesla parallel to the HERA beam. This enables the determination of the transverse momenta (in the xy-plane) with the trackers by measuring the curvature of the tracks.
- Instrumented iron return yoke (10). Its meaning is threefold:
 - it returns the magnetic field flux from the coil
 - it is instrumented to measure tracks from charged particles. This is crucial for the identification of muons.
 - it is instrumented to measure the extent of showers leaking through the main calorimeters (tail catcher)
- Forward muon device (9,11). This device consists of several drift chambers on either side of a toroidal magnet. This allows the identification of muons in the region of small polar angles $3^\circ < \theta < 18^\circ$ and the measurement of the momenta.
- Luminosity system (not visible in the figure). It consists of several scintillator detectors which measure electrons and photons in the backward region under extremely small angles. It is used to determine the luminosity and to tag electrons in photo production processes.

The components of importance in this work are described more detailed below. A complete description of the H1 detector can be found in [7].

3.2.1 The Tracking Systems

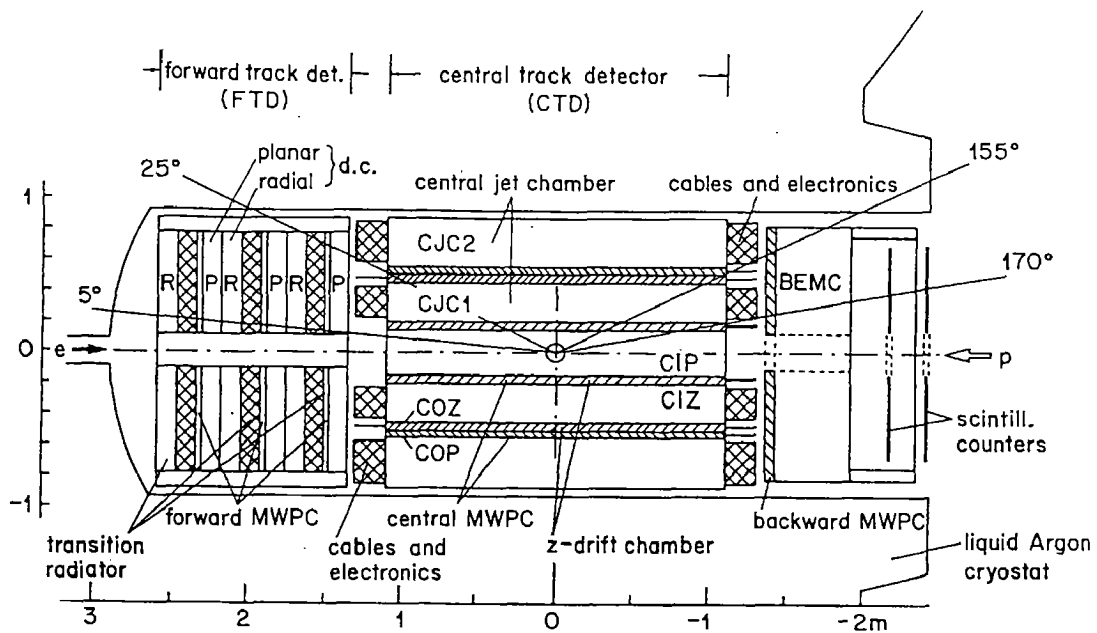


Figure 3.3: The tracking system of H1

Because of the unequal beam momenta, the track multiplicity is considerably larger at small polar angles. This fact is reflected in the design of the tracking system (see figure 3.3). It is divided in a central and a forward part.

The forward track detector consists of a set of drift chambers perpendicular to the beam axis. They are organized in three equal supermodules. Each one has a planar module with parallel wires and a radial module with wires radiating outwards from the beam pipe. In front of each module there is a multiwire proportional chamber (FPC) for trigger purpose. The parameters are:

- Angular coverage: $7^\circ < \theta < 25^\circ$
- Spatial resolution: $\sigma_{r\phi} = 170 \mu\text{m}$, $\sigma_{x,y} = 210 \mu\text{m}$

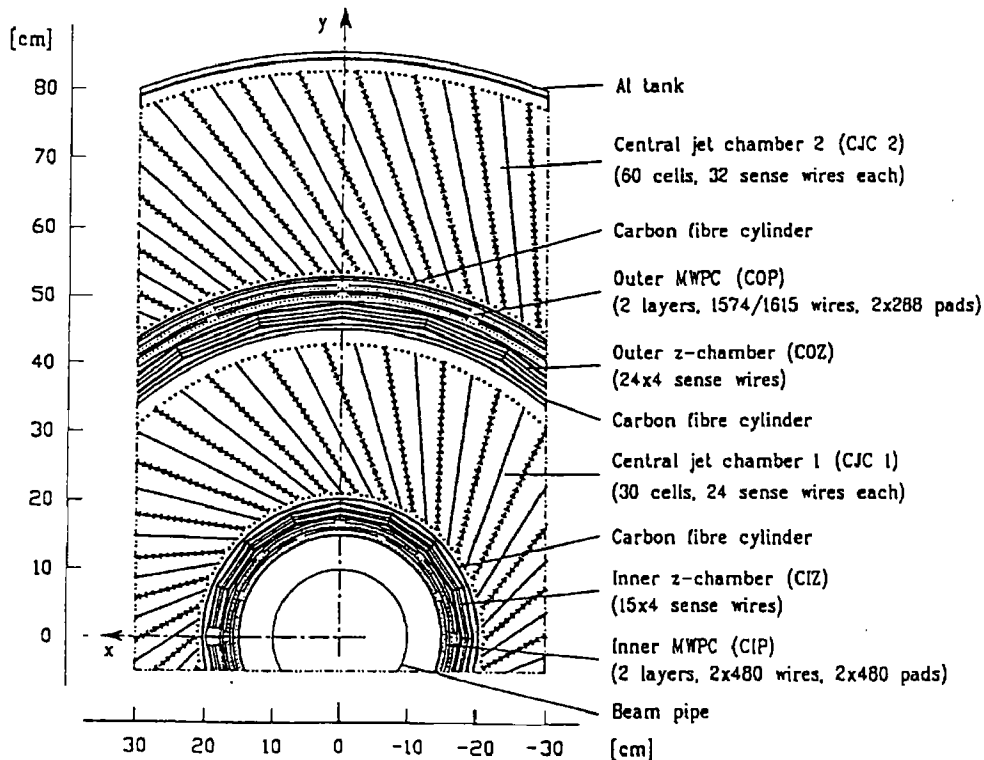


Figure 3.4: $r\phi$ -view of the central tracking device

A more detailed view of the central tracking device ([9]) is shown in figure 3.4. The main parts are two concentric drift chambers (central jet chambers CJC1 and CJC2) parallel to the beam pipe. They consist of 30 (60) drift cells with 24 (32) anode sense wires each. The cell geometry is tilted by approximately 30° with respect to the radial direction. This has several advantages:

- it optimizes the resolution for high momentum tracks, since the drift direction of the electrons in the magnetic field is approximately perpendicular to these tracks.
- the usual ambiguity of drift chambers can be resolved since the wrong track segments will not point to the event vertex and they do not match the segments of adjacent cells
- each track will cross at least one anode plane which improves the time resolution for the track

Each sense wire is read out at both ends. Through comparison of the charges at both ends one gets a relatively low z -resolution. The parameters are:

- z -resolution: $\sigma_z = 22$ mm

- $r\phi$ -resolution: $\sigma_{r\phi} = 170 \mu\text{m}$
- p_T -resolution: $\sigma_{p_T}/p_T = 0.5\% \text{ GeV}^{-1} \cdot p_T$
- dE/dx -resolution: 10%

The z -resolution from the CJC can be improved by the aim of the inner and outer z chamber CIZ and COZ. They have a resolution of $300 \mu\text{m}$. If these track segments can be linked to tracks measured in the CJC an additional fit is performed which improves the track reconstruction in the z direction.

Finally, there are two multiwire proportional chambers CIP and COP. They are not used for the track measurement, but for triggering on tracks coming from the main vertex.

3.2.2 The Calorimeters

The main calorimeter in H1 ([10]) covers an angular region of $4^\circ < \theta < 154^\circ$. It consists of eight self supporting wheels around the beam pipe. It has a sandwich structure with absorber plates and liquid argon (LAr) in the active part. The absorber material is lead in the inner (electromagnetic) part and stainless steel in the outer (hadronic) part. The thickness of the electromagnetic calorimeter varies between 20 and 30 radiation lengths, that of the hadronic part between 4.7 and 7 interaction length.

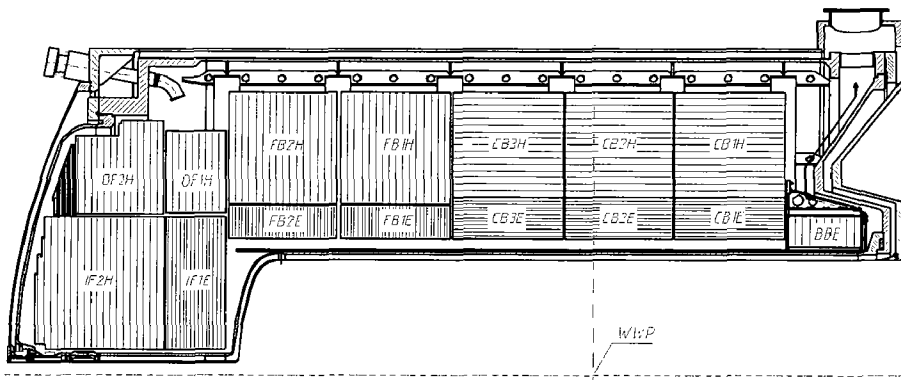


Figure 3.5: The liquid argon calorimeter

The LAr calorimeter is non-compensating calorimeter. This means, that the signal is higher for electrons/photons than for hadrons with the same energy. This has to be corrected by offline weighting technics.

The energy resolution in the electromagnetic section is $\sigma_E/E = 11\%/\sqrt{E} \oplus 1\%$ with a 3% uncertainty in the absolute energy scale. In the hadronic section it is $\sigma_E/E = 50\%/\sqrt{E} \oplus 2\%$ with a 3% uncertainty in the absolute energy scale.

3.2.3 The Muon Systems

The central muon system consists of an octagonal barrel terminated with two flat end caps. It is furthermore divided into 64 modules (see figure 3.7). Each module is built up in a sandwich structure with 10 iron plates of 7.5 cm thickness and layers of limited streamer tubes (LST). The streamer tubes have silver-coated Cu-Be wires of 100 μm diameter in it and are covered with pad or strip electrodes. Figure 3.6 shows a cross sectional view of a module. The innermost and outermost layers consist of three LST layers each, called muon boxes. Behind the fourth iron layer there are two LST layers. In the barrel region, the wires are parallel to the z -axis, while the strip electrodes are perpendicular. In the end caps the wire orientation is parallel to the x -axis and the pads are parallel to the y -axis. This gives a two-dimensional measurement for the tracks. The quality of these tracks is determined by the number and position of the LST layers which fired (see chapter 4). Only the layers directly behind an iron plate are used. The information of the pads is used to measure the energy leakage through the LAr calorimeter.

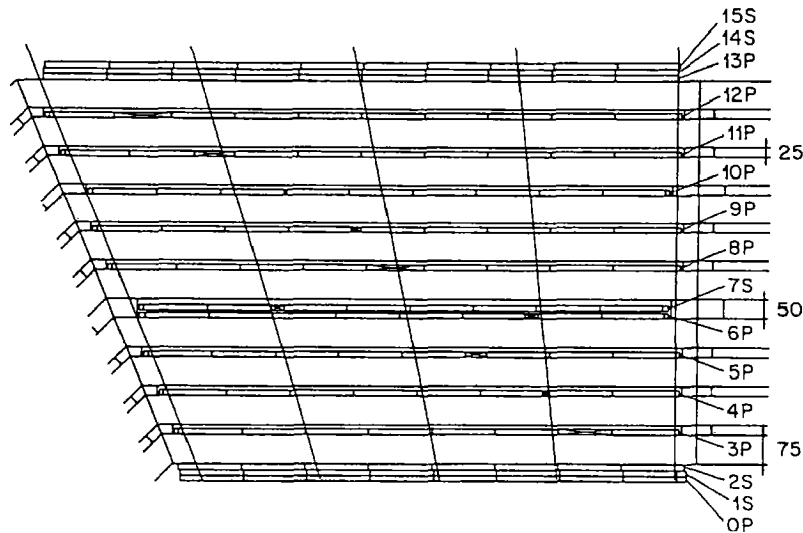


Figure 3.6: Configuration of pad and strip layers between the iron plates

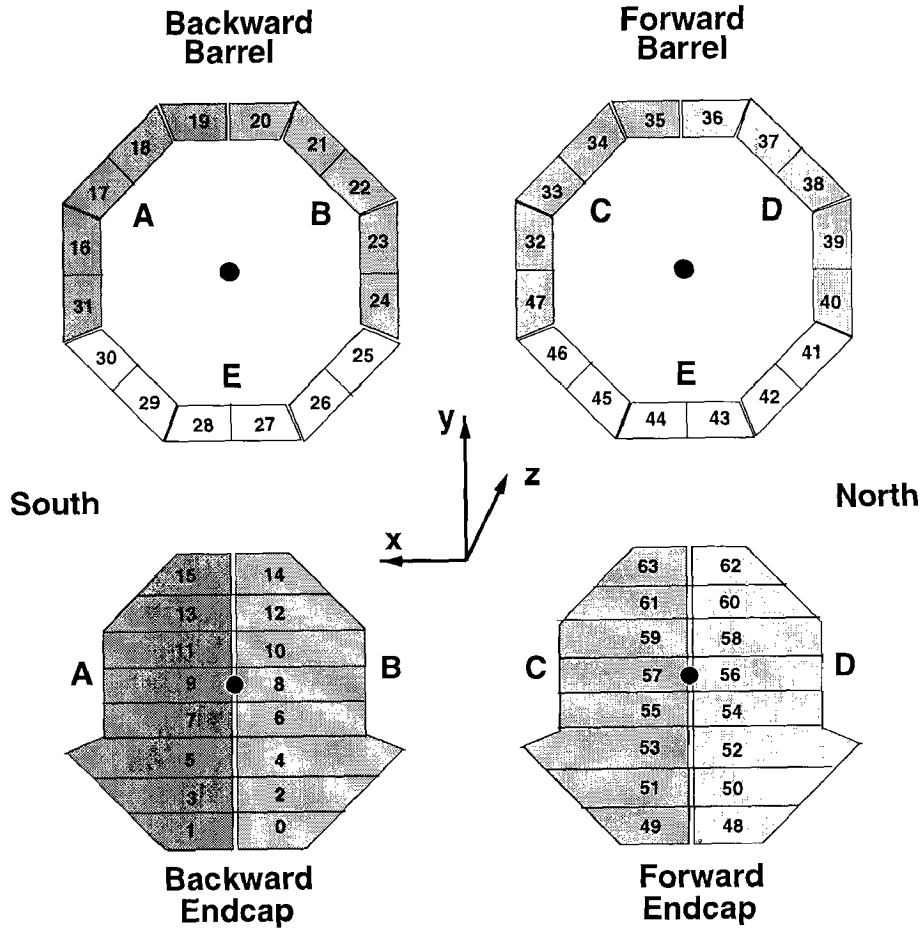


Figure 3.7: Division of the instrumented iron return yoke into modules

The parameters for the central muon system are:

- Angular coverage: $4^\circ < \theta < 17^\circ$
- Spatial resolution of the wires: $\sigma_{wire} = 3 - 4$ mm
- Spatial resolution of the strips: $\sigma_{strip} = 10 - 15$ mm
- Angular momentum resolution: $\sigma_\theta(\sigma_\phi) = 15(10)$ mrad

For the purpose of triggering the modules from figure 3.7 are grouped into 5 different regions. The assignments are:

Forward inner end cap (FIEC)	modules 54-59
Forward outer end cap (FOEC)	modules 48-53 and 60-63
Barrel (Bar)	modules 16-47
Backward outer end cap (BOEC)	modules 0-5 and 12-15
Backward inner end cap (BIEC)	modules 6-11

3.2.4 The Trigger System

HERA can produce particle collisions with a frequency of 10.4 MHz. Since the raw data size of a typical event is 100 kB, the H1 detector would produce data of the order of 1 TB/s. In order to reduce this, the trigger system selects only interesting events. The trigger device is designed in 5 levels according to decision time and information used.

- The level 1 trigger (L1) is dead-time free with a decision time of maximal 2.4 μ s. The entire event information is stored in a pipeline during this time. Subtriggers are logical combinations of information from different subdetector components, like drift chambers, calorimeters, etc. The L1 trigger signal is the logical 'OR' of these subtriggers. The dead-time starts with a positive decision of L1. The pipeline is stopped and the control is given to the level 2 trigger. The L1 output rate is 50-200 Hz. It can be adjusted to the background conditions by prescaling some of the subtriggers.
- The level 2 trigger (L2) is a set of topological triggers and neural networks. It looks for correlations in different trigger components. Its decision time is 20 μ s. It either validates the L1 decision and starts the readout of the event or it re-enables the pipeline.
- The level 3 trigger is not yet implemented. It is intended as a software trigger with a decision time of 100 μ s.
- The level 4 trigger is the last online trigger. On a farm of 33 RISC processors a fast version of the reconstruction program runs asynchronously. All information from all subsystems is available. L4 again validates the L1/L2 trigger decisions. In the year 1997 'hard scale' cuts were applied in addition. Relevant for this analysis is only the requirement of a track with $p_T > 1.8$ GeV/c. The farm can handle an input rate of 10-50 Hz and reduces the data by roughly a factor of 5. The output is written on tape as raw data.
- The level 5 trigger runs offline. It runs the full reconstruction software and divides the events into classes (e.g. heavy quark, muon class, etc.). If an

event belongs to at least one class it is stored in so called data summary tapes (DST). This is the starting point for physics analysis.

It follows the definition and description of the subtriggers used in this analysis

2.2.1.1 Definition of Subtrigger 34

On level 1 subtrigger 34 is defined as the logical 'AND' of trigger informations from the following subsystems:

- Drift chamber $r\phi$ -trigger
Required are the elements *DCRPh-Ta*, *DCRPh-TNeg* and *DCRPh-THigh*. That means, in the central region there must be at least one track with $p_{\perp} > 450$ MeV/c, at least one track of a negatively charged particle and at least one track with $p_{\perp} > 800$ MeV/c.
- Muon system
Required is the element *Mu_Bar*. This information is provided by the instrumented iron return yoke. It is defined as the coincidence of at least 2 trigger layers in the same module in the barrel region.
- z-vertex and forward ray trigger
Required are (\parallel means logical 'OR', $\&\&$ means logical 'AND'):
 - $((zVtx_mul==0 \parallel zVtx_mul==3) \&\& zVtx_T0) \parallel zVtx_Cls$
 - $((zVtx_mul==0 \parallel zVtx_mul==3) \&\& zVtx_T0) \parallel zVtx_sig$
 - $zVtx_T0 \parallel FwdRay_T0$

The trigger elements are derived from the z vertex histogram. Two hits from the CIP, COP and FPC build a track candidate. This is extrapolated to the beam axis. The z position of these hypothetical vertices is stored in the z vertex histogram.

The meaning of the trigger elements are:

zVtx_T0: there is at least one entry in the histogram

zVtx_Cls: the entries are 'clustered'. All entries are within 4 adjacent bins.

zVtx_sig: there is a significant peak in the histogram. The three criteria for the significance can be programmed and are

$$(1) \sigma_{.1} \equiv \frac{N_{max} - \bar{N}_{bg}}{\sqrt{N_{max}}} > 1.5$$

$$(2) \sigma_{\mu D} \equiv \sigma_{.1} \vee (6 \cdot N_{max} > N_{sum} + 3) \text{ } ^1$$

¹used only in the year 1997

- (3) σ_{net} is optimized for triggering leptonic decays of J/Ψ mesons. The cuts were determined with a neural net.

Here N_{max} is the maximum number of entries in one bin, \bar{N}_{bg} is the average number of entries in the other (background) bins and N_{sum} is the sum over all bins.

zVtx_mul: to each event there is assigned a multiplicity code. The assignment can be found in [11]. It is used to reject events with very high track multiplicities.

FwdRay_T0: timing information from the forward ray trigger.

- Time-of-flight system (ToF)
Required are (! means logical 'NOT'):

!BToF_BG and (*FToF_IA* || *!FToF_BG*)

The ToF system consists of two scintillator planes both in the forward (FToF) and backward (BToF) region. The timing information is used to define time windows for ep-interaction (*xToF_IA*) and for background events (*xToF_BG*). Thus these trigger elements reject events from non-ep interactions.

- Veto walls
Required are *!VETO_Inner_BG* and *!VETO_Outer_BG*
Similar to the ToF the timing information from the veto walls (double scintillator walls in the forward region) is used to reject events from non-ep interactions.

No trigger requirement is applied on level 2.

2.2.1.1 Definition of Subtrigger 15

On level 1 subtrigger 15 is defined as the logical 'AND' of trigger informations from the following subsystems:

- Drift chamber $r\phi$ -trigger
Required is the element *DCRPh_THigh* explained above.
- Muon system
Required is the logic 'OR' of the following elements:
 - *Mu_Bar*
 - *Mu_FOEC*
 - *Mu_BOEC*
 - *Mu_BIoOEC*

The second and third element is the coincidence of three trigger layers in the forward and backward outer endcap respectively. The last element is the coincidence of two trigger signals in the backward inner or outer endcap.

- z vertex trigger

Required is: $zVtx_sig$

- Time-of-flight system

Required is: $(!FToF_BG \parallel FTof_IA) \&\& !BToF_BG$

- Veto walls

Required is: $!VETO_Inner_BG \&\& !VETO_Outer_BG$

- Spacal

Also the Spacal provides a timing information to reject events outside the nominal bunch crossing time. The trigger elements required are:

– $!SPCLh_AToF_E1$

– $!SPCLe_AToF_E1$

– $CIPB_noSPCLe_T_E1 = CIP_Backward + !SPCLe_ToF_E1$

The first two elements are cuts on the energy measured in the background time window for the hadronic and electromagnetic parts of the Spacal. The last element requires that there is no energy deposited in the electromagnetic Spacal within the interaction time window, but the CIP has a signal in the backward region.

On level 2 a neural network trigger is applied, which is optimized for triggering J/Ψ mesons decaying into two muons.

2.2.1.1 Definition of Subtrigger 87

On level 1 subtrigger 87 is defined as the logical 'AND' of trigger informations from the following subsystems:

- Drift chamber $r\phi$ -trigger

Required are the elements $DCRPh_Ta$ and $DCRPh_T0$ explained above.

- Muon system

Required is the element Mu_Any which is the logic 'OR' of the following elements:

– Mu_Bar

– Mu_BIEC

- *Mu_BOEC*
- *Mu_FIEC*
- *Mu_FOEC*

The last 4 elements are the coincidence of three trigger layers in the forward (backward) inner (outer) endcap respectively.

- Luminosity system
Required is the logical 'OR' of
 - *eTAG*, a hit in the e-tagger at $z=-33.4\text{m}$
 - *LU_ET_8 && !LU_PD*, a signal in the e-tagger at $z=-8.0\text{m}$ with a veto in the photon detector (in 1997 only)
 - *LU_ET_44 && !LU_PD_low && !LU_WatVet*, a signal in the e-tagger at $z=-43.2\text{m}$ with a veto of the photon detector and the water Čerenkov detector
- z vertex trigger
Required is: $zVtx_T0 \parallel FwdRay_T0$
- Time-of-flight system
Required is: $(!FToF_BG \parallel FToF_IA) \&\& !BToF_BG$
- Veto walls
Required is: $!VETO_Inner_BG \&\& !VETO_Outer_BG$
- Spacal
Required is *!SPCLh_AToF_E_1* explained above

There is no level 2 condition to be fulfilled.

Chapter 4

Data Selection

This chapter explains how the data is selected. Two muons are required in this analysis. In order to identify a muon in the detector, one has to study different components of the detector. Sections 1 and 2 describes how tracks and energies are measured. Section 3 shows how muons are identified and how efficient this can be done. In section 4 the final data selection cuts are presented. The selection efficiency is determined in section 5. To measure a cross section one has to know the trigger efficiencies (section 6) and the luminosity (section 7). In section 8 a picture of an elastic and an inelastic event is shown.

4.1 Track Selection

A track inside the superconducting coil is modeled as a helix. Its parameters are:

- d_{ca} , the distance of closest approach from the track to the primary vertex. It is positive if the vectors \mathbf{d}_{ca} , \mathbf{p}_T and the z-axis form a right handed system.
- ϕ_{dca} , the azimuthal angle and
- z_{dca} , the z coordinate at the d_{ca} -point
- θ , the polar angle of the track
- κ , the curvature. It is the inverse of the radius of the track. The sign is the opposite of the sign of the charge. The transverse momentum p_T is obtained from this via

$$p_T = \frac{0.3 \cdot q \cdot B}{\kappa},$$

where B is the magnetic field strength.

A circle is fitted in the $r - \phi$ -plane to determine κ , d_{ca} and ϕ_{dca} , while z_{dca} and θ are obtained by a least squares fit in the $r - z$ -plane. The results are so called non vertex fitted tracks.

To improve the accuracy further, these tracks are fitted to vertices. There may be different hypothesis according to (a) fittings to different vertices (primary, particle decay vertex, or nominal run vertex) and (b) different parameterization due to multiple scattering between the inner and outer CJC. Hypothesis are removed by selecting tracks from the primary vertex in favour of tracks from the run vertex. Decay vertices are rejected in this analysis. In addition the following quality cuts must be fulfilled:

Central tracks	
Minimum p_T	150 MeV/c
Minimum θ	20°
Maximum θ	160°
Maximum $ d_{ca} $	2 cm
Maximum radius of track start	50 cm
Minimum track length	10(5) cm for $\theta < 150(160)^\circ$

In the limited angular region of $\theta \in [20^\circ, 25^\circ]$ tracks can be measured partly in the central tracker and partly in the forward tracker. Such tracks are called combined tracks. The quality cuts for these tracks are:

Combined tracks	
Minimum p_T	150 MeV/c
Minimum θ	20°
Maximum θ	40°
Maximum $ d_{ca} $	5 cm
Maximum radius of track start	50 cm
Maximum χ^2 of central-forward link	50.0
Maximum χ^2 of DTRA track fit	50.0
Maximum dp/p	1.0

In case of ambiguities combined tracks are preferred to central tracks. Tracks measured in the forward tracker only are not considered here. The reconstruction efficiencies for vertex fitted tracks have been investigated in [17] and are modeled very well in the detector simulation. The discrepancy is $\sim 3\%$ and is taken as a systematic error.

4.2 Energy Measurement

Energy measurement in the calorimeter plays a subsidiary role in this analysis. It is used for the identification of muons and for the detection of the hadronic final state. The LAr is a non-compensating calorimeter which means that for electromagnetic showers the charge output is higher than for hadronic showers with the same initial energy. Thus, a weighting scheme is introduced and it is important to recognize a shower either as a hadronic or an electromagnetic one.

Energy is measured in individual cells. After applying noise reduction cuts, a correction for dead material in front of the first cells is determined and the corresponding energy is added to these cells. Adjacent cells above threshold are then grouped into clusters. Only clusters with

$$\sqrt{\sum_{cells} \left(\frac{E_i}{\sigma_{noise}}\right)^2} \geq 8 \quad (4.1)$$

are considered further. E_i is the energy in the i -th cell of the cluster and σ_{noise} is the width of the energy deposition for empty events. A cluster is then classified as electromagnetic if its energy is at least 1 GeV, most of it (80%) is found in the electromagnetic part of the LAr, it is well inside an octant and there is a high electron identification probability based on the energy distribution inside the cluster. It is classified as hadronic if (a) it is not electromagnetic and (b) for energies < 1 GeV the center of gravity must be located at least 1/3 radiation length inside the calorimeter or the energy is not concentrated in very few cells. For more details see [12].

Three energy scales are defined

- **AE0R scale:** electromagnetic energy deposited in a homogeneous calorimeter.
- **AE1R scale:** electromagnetic energy after applying the correction for dead material.
- **AEFR scale:** energy deposited by hadrons. The correction for the non-compensating nature of the LAr calorimeter is applied. This scale is used for the identification of muons and for measuring the hadronic final state.

4.3 Muon Identification

There are two possibilities to identify muons in the central region. Muons with an energy of a few GeV pass the calorimeters as minimum ionizing particles in contrast to other charged leptons or hadrons. This gives us two possibilities to identify them: (a) since they penetrate the calorimeter, they leave signals in the instrumented iron

return yoke. Tracks are fitted to these hits, which then are linked to tracks of the inner tracker. (b) Since they are minimum ionizing they leave only a small amount of energy in the calorimeter. This energy is concentrated close to the line of flight of the muon. This signature of energy deposition is typical for muons, and thus is a possibility to identify them. The two methods are discussed here.

4.3.1 Muon Reconstruction in the Instrumented Iron

Muons passing through the instrumented iron return yoke leave signals in the limited streamer tubes (see chapter 3). A pattern recognition program groups hits belonging to the same track to form so called associations. After applying some quality cuts, parabolas are fitted to these associations (for more details see e.g. [12],[13]). The track parameters are

- coordinates of the first (innermost) hit
- track direction at this point
- ratio of charge/momentum

These parameters together with the errors, number of hits and an estimation of the quality of the fit are stored as '*muon tracks*'. Additional quality cuts can be applied to these tracks. Important measures for the quality are the number of layers that are used to define the track and the first and the last layer which are used. In this analysis the following standard cuts are used:

	max first layer	min last layer	min # of layers
Barrel region	5	2	2
Forward endcap	5	6	6
Backward endcap	8	3	3

In order to identify a muon through its penetration capability, such a track has to be linked to a 'good' inner track as described in section 1. Inner tracks with $p_T > 1$ GeV/c are extrapolated to the iron system under the assumption of a minimum ionizing particle. A muon track is linked if it is close enough to this extrapolation. This means:

$$|\theta_{innertrack} - \theta_{muontrack}| < 0.2 \text{ rad}$$

$$-\frac{\pi}{2} < (\phi_{innertrack} - \phi_{muontrack}) < 0.2 \text{ rad, if } \kappa > 0$$

$$-\frac{\pi}{2} < (\phi_{muontrack} - \phi_{innertrack}) < 0.2 \text{ rad, if } \kappa < 0$$

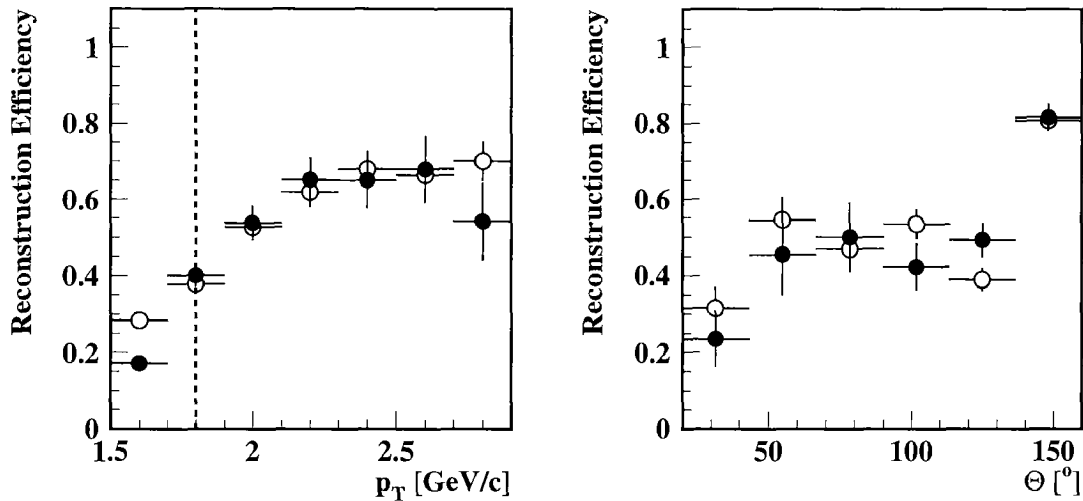


Figure 4.1: Reconstruction efficiency for muons in the instrumented iron as a function of p_T and Θ . Solid circles denote data, open circles denote MC. The dashed line indicates the cut in the final data selection. This cut on $p_T > 1.8$ GeV is applied in the figure on the right.

where κ is the curvature of the track. The asymmetric cut on ϕ allows a larger deviation in the direction of the curvature. There are in general several links with the same muon or inner track. A link probability is calculated according to a χ^2 distribution, where χ^2 is defined through

$$\chi^2 = (\vec{X}_E - \vec{X}_I)^T V^{-1} (\vec{X}_E - \vec{X}_I)$$

\vec{X}_E stands for the track parameters of the extrapolated track, \vec{X}_I are the parameters of the iron track and V is the covariance matrix. To avoid double counting of muons only the hypothesis with the highest link probability is chosen. This probability has to be greater than 0.1%. For more details see [14].

The reconstruction efficiencies for muons identified in the iron system is estimated from a Monte Carlo simulation. It has been verified with data containing the J/Ψ peak. The idea is the following. Select events with exactly two reconstructed tracks which have an invariant mass around the J/Ψ peak. If one track is well identified as a muon, then the other track is also a muon with a very high probability (coming from the J/Ψ decaying into two muons). The reconstruction efficiency is just the fraction of events with secondary tracks which are identified as muons divided by the total number of events. The result of such an analysis is shown in figure 4.1.

Data and Monte Carlo simulation are in good agreement above $p_T \approx 1.8$ GeV/c. This is the cut used in the final event selection (section 4). Below this threshold the description of the energy loss is very sensitive to the exact description of the material in front of the iron.

The misidentification of hadrons (mainly π and K) as muons was investigated in [29]. Above a momentum of 2 GeV/c, it is of the order of 0.5-1% for pions and 2% for kaons. In [29] these numbers are derived from Monte Carlo simulation. This has been checked for pions with data, where the decay of $K^0 \rightarrow \pi\pi$ is reconstructed. The agreement is very good.

4.3.2 Muon Reconstruction in the LAr Calorimeter

Muons can be identified by the signature of a minimum ionizing particle in the LAr calorimeter. It follows a description of the method.

A track is extrapolated into the LAr calorimeter and two cylinders of radius 15 and 30 cm around the track are defined (see figure 4.3.2).

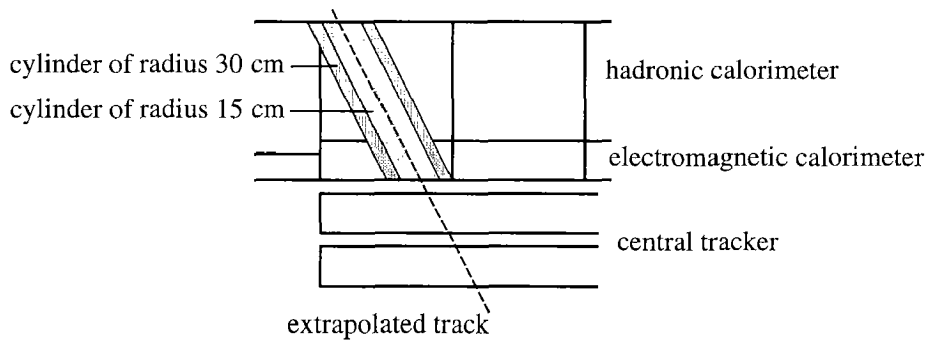


Figure 4.3.2: definition of the cylinder around the extrapolated helix

The following quantities are defined

- E_{EM} is the total electromagnetic energy within the inner cylinder. The energy from the individual cells e_i are weighted with a function h_i which is 1.0 inside the cylinder and falls off exponentially outside.
- E_{tot} is the total energy (weighted with h_i) within both cylinders.
- $L_{max} = \max\{l_j h_j\}$ where l_j is the maximum distance of a cell beyond threshold in the inner cylinder from the entry point of the track into the calorimeter.
- $L_{HAC} = \sum_{HAC} l_j h_j$ is the weighted sum in the inner cylinder in the hadronic calorimeter.

Cuts are applied to these quantities depending on the energy and polar angle. The mean values for the central region are

Variable	lower limit	upper limit
E_{EM}	0.1 GeV	0.8 GeV
E_{tot}	0.4 GeV	2.4 GeV
L_{max}	80 cm	-
L_{HAC}	150 cm	-

The cuts are not strict but smeared in the sense that the cut is made only to the normalized sum of the deviations from these cut values. The value of this sum defines three quality classes for muons. One has to make a compromise between the reconstruction efficiency and the misidentification rate for pions. In this analysis medium and good muon candidates are selected which restricts the misidentification rate to 5-10% depending on the angular range. For more detail about lepton identification in the LAr calorimeter see e.g. ref. [15].

The reconstruction efficiency for calorimeter muons have been checked with MC. Tracks identified in the iron as muons were selected. The fraction which were identified in the calorimeter is an estimate for the reconstruction efficiency. A discrepancy between data and MC of $\approx 14\%$ was seen. This is independent of energy and polar angle and is in agreement with other studies [20]. A more detailed study of the scaling, calibration and noise suppression for the LAr cells is needed. This is beyond the scope of this work. Therefore an overall correction factor has been applied to the MC. The result is shown in figure 4.3.2. The reconstruction efficiency has been determined to 78.1%.

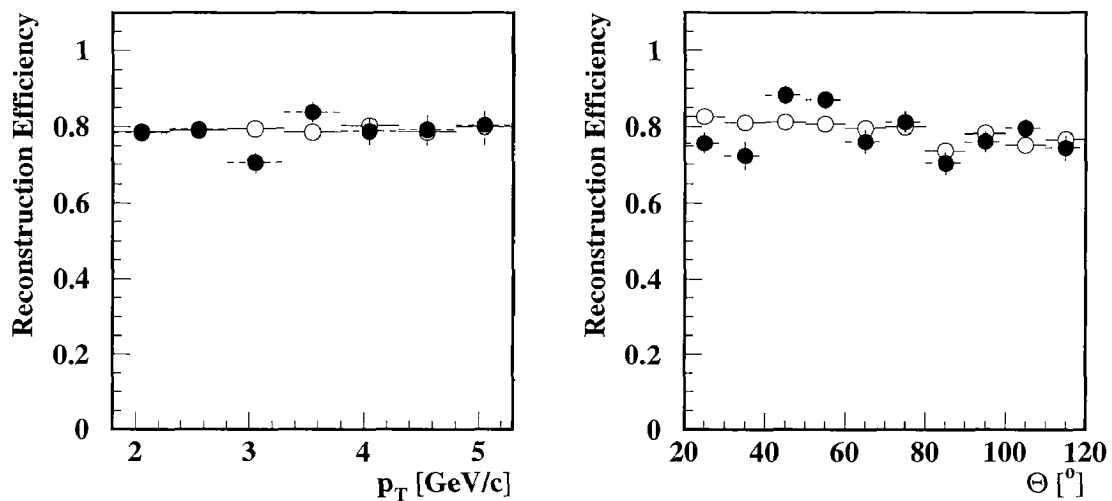


Figure 4.3.2: Reconstruction efficiency for muons in the LAr calorimeter as a function of p_T and Θ . Solid circles denote data, open circles denote MC. The later is corrected for its overestimated reconstruction efficiency (see text).

4.4 Event Selection

We are now ready to list the data selection criteria. In this section the applied cuts are listed and explained afterwards.

The data has been recorded during the years 96 and 97, corresponding to $61.0 \cdot 10^6$ events.

The first cut addresses the data quality:

1. All relevant subdetector components must have been fully operational (see section 4.7 for details)

In this analysis two high energetic muons with a high invariant mass are requested. The following muon selection cuts have been applied:

2. Number of reconstructed muons = 2. At least one of them must be reconstructed in the barrel region of the instrumented iron. The other one may be a calorimeter muon and/or an iron muon.
3. $20^\circ \leq \theta \leq 160^\circ$ for both muons.
4. $p_T \geq 1.8 \text{ GeV}/c$ for both muons
5. The invariant mass of the two muons is larger than $5 \text{ GeV}/c^2$

The remaining data sample consists of 694 events. The main background sources are cosmic muons and muons from heavy quark decays. They are effectively rejected by the following cuts

6. The two muons are well separated from the hadrons. The criterion is $R \equiv \sqrt{\Delta\eta^2 + \Delta\phi^2} \geq 1.0$, where $\Delta\eta$ and $\Delta\phi$ are the distances to the closest track or energy cluster in pseudorapidity and azimuthal angle respectively.
7. The opening angle of the two muons is less than 165°
8. The time as reconstructed in the jet chamber, must be within 5 ns around the nominal bunch crossing time given by the RF-signal from the accelerator.
9. The reconstructed z coordinate of the primary vertex must be in the range [-30 cm, +20 cm]

The remaining number of events is 368. Finally a set of subtrigger has to be selected:

10. The event must have been triggered by the subtriggers 15, 34 or 87 according to table 4.7

This leaves us 278 events. In addition, for the data set of **elastic** events, no signal must have been seen in the forward detectors. That is

11. The energy in the LAr calorimeter deposited below $\theta = 15^\circ$ must be smaller than 300 MeV

12. Number of hit pairs in the forward muon detector (FMD) must be less than 2
13. No hits are found in the proton remnant tagger

Events which fail one of the cuts 11 to 13 add to the set of **inelastic** events. We end up with 144 elastic and 134 inelastic events. None of these events have two muons with like sign charges.

Cuts 2 to 5 define the event topology and the kinematic range under investigation. The muon in the barrel of the iron is required to ensure that the event is in the acceptance for the subtriggers. The p_T cut makes sure, that the value for the muon reconstruction efficiency is on its plateau, where it is understood.

Cuts 6 to 9 are used to reject background. Cut 6 rejects open heavy quark production events, where the muons are within the jet. Cuts 7 to 9 reject cosmic muon events, where the tracks are reconstructed in a back to back configuration or either the time is uncorrelated to the HERA clock or the vertex z coordinate is outside the nominal bunch crossing region. The rejection power of cuts 6 and 7 can be seen in chapter 6 where the background is investigated. In cut 10 three different subtriggers are selected. In order to calculate a cross section, the trigger efficiency has to be known. Therefore, one has to restrict the number of subtriggers used. From the 128 existing subtriggers, the three by far most efficient subtriggers have been chosen. The rest of the cuts is self explanatory. In addition, a set of topological halo muon finders have been used. They are part of the H1PHAN physics analysis package and are described in [18]. Their performance is very good in the sense that no events from Monte Carlo simulation has been rejected and after visual inspection of the remaining data events, no candidate for a halo muon event has been found. Thus, their efficiencies is assumed to be 1.

In table 4.1 the cuts are summarized and the number of events remaining after the cut is shown.

At the end of this chapter you can see a picture of a typical elastic and an inelastic event.

In figure 4.2 the distribution of transverse momentum p_T^μ of the muons, the polar angle θ^μ of the muons, the invariant mass $M^{\mu\mu}$ and the z vertex position is shown. It is compared to the Monte Carlo simulation.

4.5 Selection Efficiency

As a last ingredient we have to know the acceptance and the efficiency of the data selection. The distinction of the two is not strict and only the product of the two is relevant. In this analysis it is handled as follows. The acceptance $A_{el,in}$ for the elastic or inelastic cross section respectively is defined by the cuts

- $20^\circ \leq \theta \leq 160^\circ$ for both muons

Cut	Number of events	
Number of muons = 2 (one in the barrel) ¹	1151	
$20^\circ \leq \theta \leq 160^\circ$ for both muons	1148	
$p_T > 1.8$ GeV for both muons	832	
Invariant mass > 5 GeV	694	
Separation $R > 1.0$	453	
Opening angle $\theta^{\mu\mu} < 165^\circ$	391	
Track time and z vertex cut	368	
Subtrigger on	278	
All cuts	elastic	inelastic
	144	134

Table 4.1: Summary of the data selection cuts and number of events after applying the cuts consecutively. The detector had to be fully operational.

- $p_T \geq 1.8$ GeV/c for both muons
- $M^{\mu\mu} \geq 5$ GeV/c²

This defines a *visible* cross section σ_{vis} through

$$\sigma_{vis}^{el,in} = A_{el,in} \cdot \sigma_{tot}$$

where σ_{tot} is the total cross section. Here only the visible cross section is measured. The extrapolation to the full cross section adds new systematic uncertainties and therefore is not done. The acceptance/efficiency of all the other cuts is packed into the term 'selection efficiency' and is denoted by ϵ_{sel} . This is estimated from a Monte Carlo simulation via

$$\epsilon_{sel} = \frac{N_{sel}^{mc}}{N_{acc}^{mc}}$$

where N_{sel}^{mc} is the number of generated events passing the cuts 1 to 10 and N_{acc}^{mc} is the number of generated events within the acceptance region, that is, passing the 3 cuts above.

To do this, it is crucial that the relevant kinematic distributions are in good agreement between data and Monte Carlo simulation. The relevant variables are θ and p_T of the muons, the z coordinate of the vertex and the invariant mass. The agreement between data and Monte Carlo simulation is fairly good as shown in figure 4.2.

The distinction into elastic/inelastic events in data is done via the cuts 11 to 13. We will have to define what we really mean with *elastic* or *inelastic* and how data is compared to Monte Carlo simulation. This is deferred to chapter 5 where this is defined and explained in detail.

Table 4.2 summarizes the different contributions to the selection efficiency.

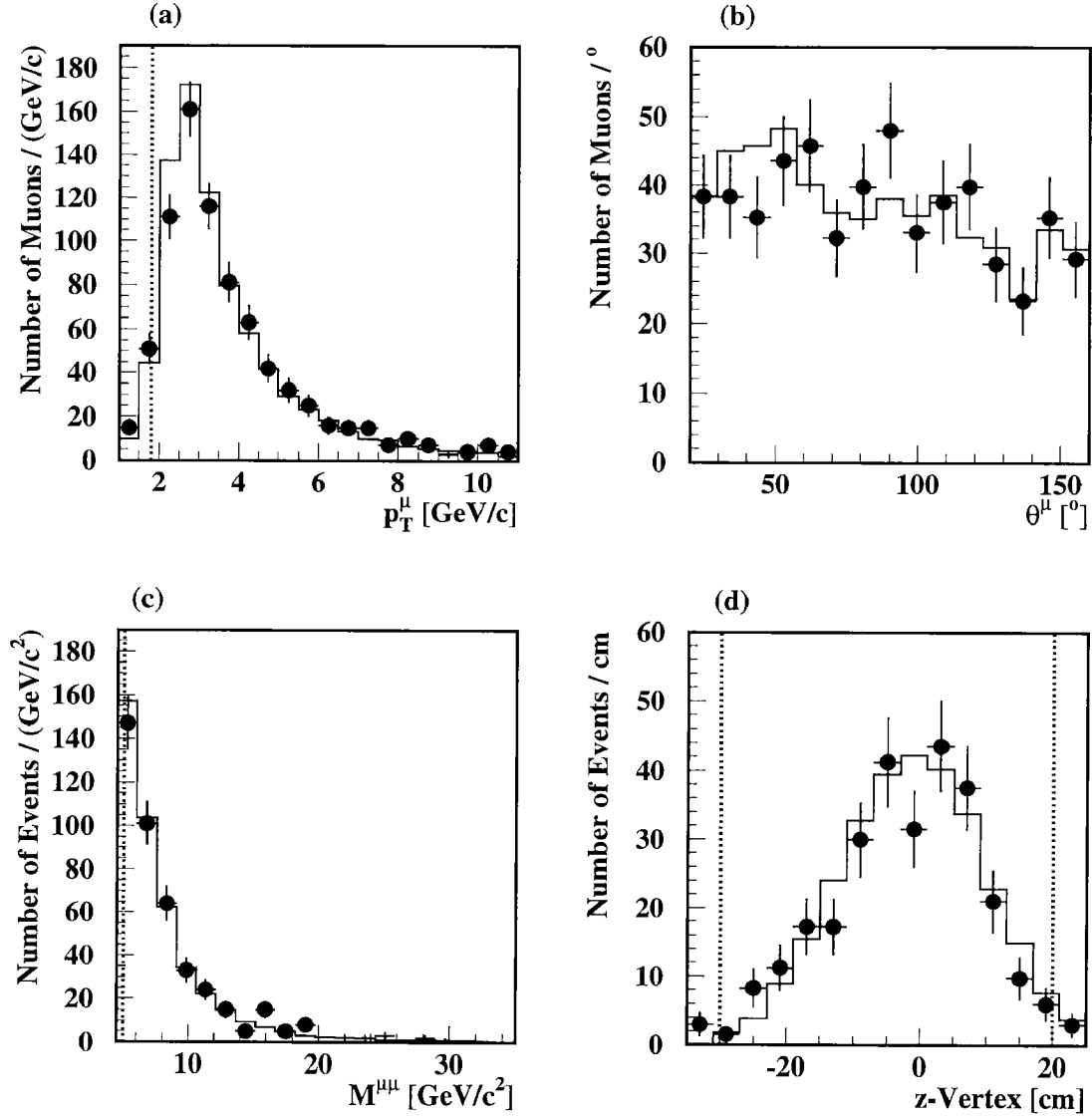


Figure 4.2: Distribution of the transverse momentum (a) and polar angle (b) of the muons, the invariant mass of the two (c) and the z coordinate of the primary vertex (d). The points show data, the histograms show Monte Carlo simulation. Shown are the sum of the years 96 and 97. The discrepancy between the two years is very small. All cuts are applied except the cut on the variable which is plotted. The cuts are indicated by a dotted line. The agreement between data and Monte Carlo simulation is quite good.

Cut	96	97
Number of muons = 2 (one in the barrel)	59.0%	58.2%
$p_T > 1.8$ GeV/c for both muons	95.5%	95.4%
Separation $R > 1.0$	99.5%	99.0 %
Opening angle $\theta^{\mu\mu} < 165^\circ$	89.0%	89.0%
Track time and z vertex cut	97.6 %	96.9%
Total	48.7 %	47.4 %

Table 4.2: Summary of the selection efficiencies. Since the acceptance cannot strictly be separated from the efficiency, both is included in the term 'efficiency' here.

4.6 Trigger Efficiencies

As mentioned in chapter 3, the trigger system of H1 is built up in 5 levels. The trigger requirements on the levels 1 and 2 for the subtriggers used in this analysis are described there. In this section the efficiencies for all relevant trigger levels are investigated. During the 1996 data taking period the subtriggers 34 and 87 were used. In addition to this in the second half of the year 1997 the subtrigger 15 was added.

4.6.1 Trigger Efficiencies on Level 1

The trigger efficiency has been determined from Monte Carlo studies. Aside from a total detector simulation, the H1 simulation software package contains a simulation of most of the level 1 trigger elements. The simulation of the detector has been tuned to describe data as close as possible. This holds especially for the triggers. However, this tuning is done with much more inclusive data samples. Thus, one has to check for eventual discrepancies between the real and simulated trigger efficiencies for the data selected in this work. Figures 4.3 and 4.4 show the efficiencies for the main trigger elements for sets containing both elastic and inelastic events. As can be seen, Monte Carlo simulation and data are in good agreement. The efficiencies did not change significantly between the years 96 and 97. The trigger elements are not sensitive to track multiplicities and hence do not distinguish between elastic and inelastic events. The results can be found in the summary table 4.3. The error is estimated from the discrepancy between data and MC.

Studies for the zVtx trigger showed, that MC describes data well. The result can be found in the summary table. Trigger elements not shown in table 4.3 have been studied elsewhere and have efficiencies close to 1.

Trigger Prescale

Because of limited bandwidth and computing power, the input rate on level 4 is lim-

TE	Efficiency in %
Mu_Bar	96.5 ± 3.1
Mu_ECQ	86.5 ± 5.6
Mu_Any	97.3 ± 1.3
DCRPh_THA	97.2 ± 2.1
DCRPh_TNeg	96.0 ± 3.3
DCRPh_THig	97.2 ± 2.1
DCRPh_T0	97.0 ± 2.0
zVtx_T0	97.2 ± 3.1
zVtx_Cls	96.2 ± 3.8
zVtx_Sig	96.3 ± 1.2
zVtx_mul	96.0 ± 2.3
FwdRay_T0	92.0 ± 5.0

Table 4.3: Summary table for the trigger level 1 efficiencies. Shown are the efficiencies for the individual trigger elements. The efficiencies were constant during the years 96 and 97. The errors are estimated by comparison with data.

ited to ~ 50 Hz in order to keep the dead-time low. L1 subtriggers with high rates are prescaled depending on the luminosity and the beam condition. This prescale has to be included in the level 1 trigger efficiency. The different prescale factors can be found in table 4.4 together with the total level 1 efficiencies.

4.6.2 Trigger Efficiencies on Level 2 and 4

On level 2 subtrigger 15 is kept or rejected based on the output of a neural net, while the subtriggers 34 and 87 pass unaltered.

On level 4 a verification of the level 1 and 2 decisions is performed. This is based on an online (partially simplified) reconstruction of the full event. Events are kept, if at least one subtrigger is confirmed. In addition to this, in the year 97 'hard scale' cuts were applied to the remaining events. An event is kept if e.g. a track with $p_T > 1.8$ GeV/c has been found. Since this is required by the data selection cuts anyway (see section 4), this does not add an inefficiency².

Subtrigger 34

To confirm subtrigger 34 a track in the instrumented iron has to be linked to a track in the inner tracker. The efficiency of this matching has to be determined from data, since there is no simulation of level 4. This has been done with a data set similar to the final data selection (section 4) with the following cuts loosened:

²or better: the inefficiency is already included in the reconstruction efficiency

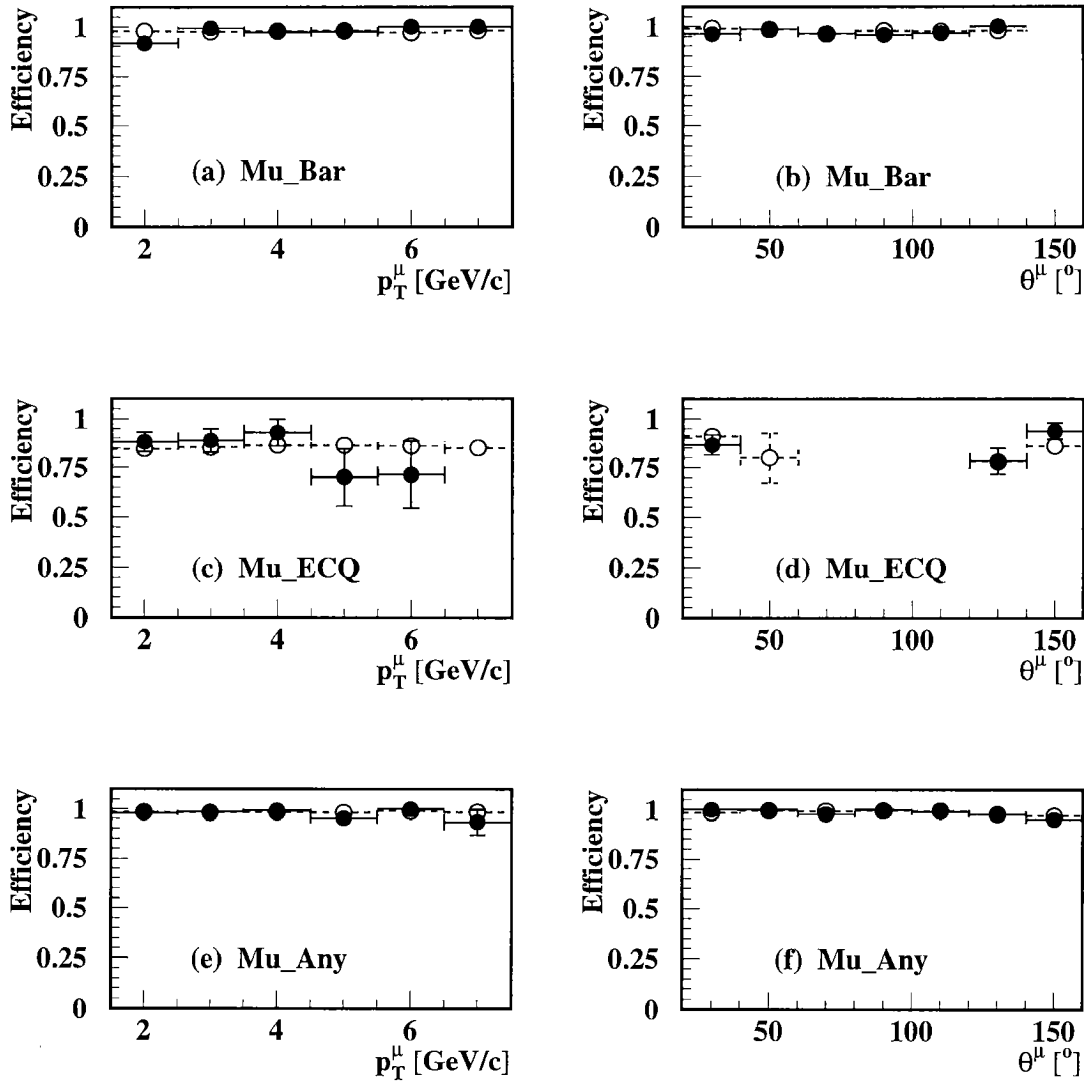


Figure 4.3: Efficiency of the trigger element Mu_Bar as a function of transverse momentum (a) and azimuthal angle (b) and the same for the trigger element Mu_ECQ (c),(d). Open circles denote MC and solid circles denote real data.

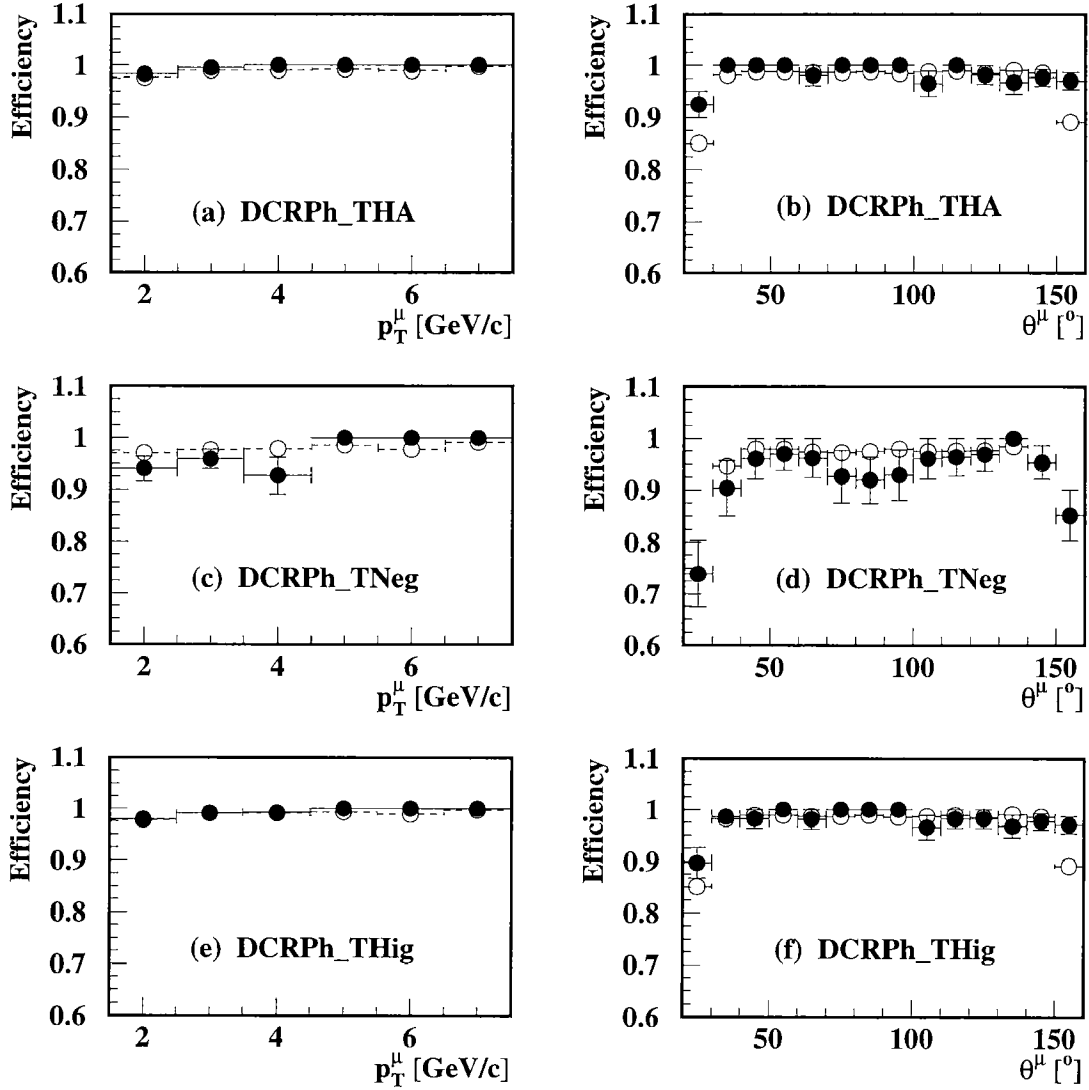


Figure 4.4: Efficiency as a function of transverse momentum and azimuthal angle of the trigger elements DCRPh_THA (a,b), DCRPH_TNeg (c,d) and DCRPh_THig (e,f). Open circles denote MC and solid circles denote real data.

- no cut on the invariant mass
- opening angle $< 175^\circ$
- no cut on the charges

The matching does not depend on these cuts. A set of subtriggers which is independent of the muon system has been chosen. From this data set of 192 events an efficiency of $92.2 \pm 1.9\%$ has been calculated. The result for 96 is $89.7 \pm 3.9\%$.

Subtrigger 15

For the verification of subtrigger 15 a reconstructed track in the iron system has to be found. Since this is required in the selection, the level 4 efficiency is expected to be 100%. However, only the combined level 2/4 efficiency can be determined from data. This has been done with a data set with the same cuts as above. The efficiency is $69.1 \pm 4.0\%$.

Subtrigger 87

The level 4 efficiency has been determined from data using independent subtriggers. The cuts has been loosened, similarly to subtrigger 34, since there is no dependency of the efficiency on them. The result is $96.9 \pm 1.5\%$

From data no correlation has been found between events with different subtriggers rejected on level 2/4. Thus, the inefficiencies are simulated randomly and independently. The total trigger efficiencies can be found in table 4.4. These efficiencies hold on a data set with all selection cuts applied. Three run ranges are defined. The first one corresponds to the 96 running period. The second one corresponds to the first part of the 97 running period where only subtriggers 34 and 87 were active. In the second half of the year 97 the combination of the subtriggers 15, 34 and 87 was used.

4.7 Luminosity

For the correct normalization of the cross section we have to know the integrated luminosity. In H1 the instantaneous luminosity is measured via the bremsstrahlung process $ep \rightarrow e\gamma p$. This process has a very high cross section, thus leading to a small statistical error. The e and γ are measured in coincidence by two Čerenkov detectors. These are the electron tagger at $z = -33.4$ m and the photon detector at $z = -102.9$ m.

Several corrections have to be applied:

Year	96	97	97
Run range	146416 - 171156	184258 - 193432	193433 - 200406
Subtrigger	34 \vee 87	34 \vee 87	15 \vee 34 \vee 87
Level 1	45.8 \pm 3.8	63.9 \pm 5.4	82.7 \pm 6.5
Level 2/4	92.6 \pm 4.0	94.7 \pm 2.0	96.4 \pm 5.9
Total	42.4 \pm 4.0	60.5 \pm 5.3	79.7 \pm 8.0

Table 4.4: Trigger efficiencies for the 3 trigger levels in %. For the reference data set all selection cuts are applied. The three run ranges correspond to different years and/or trigger setups as indicated above. The last line shows the total trigger efficiencies.

- **Background bremsstrahlung processes**

The main background source is the bremsstrahlung process $eA \rightarrow e\gamma A$, where A is the nuclei of a residual gas atom in the beam pipe. This background rate is estimated by measuring the rate for electron pilot bunches (beam crossings where the proton bunch is empty). The statistically corrected luminosity is

$$\mathcal{L} = \frac{R_{tot} - (I_{tot}/I_p)R_p}{\sigma_{vis}} \quad (4.2)$$

Here R_{tot} and R_p are the total bremsstrahlung rate and the rate for e pilot bunches respectively. I_{tot} and I_p are the corresponding electron beam currents and σ_{vis} is the visible part of the bremsstrahlung cross section. The latest includes acceptance and efficiencies. This correction is done online. The following corrections are done offline.

- **Satellite bunch correction**

The proton beam is made up of bunches. These bunches show a substructure with a main peak and two smaller ones. The later are off in time by ± 5 ns and are called satellite bunches. The reconstruction for events from satellite bunches is not optimized. Thus events are excluded by a cut on the z-coordinate of the main vertex. Since the time resolution of the luminosity system is lower (20 ns), a bremsstrahlung event cannot be assigned to one of the three peaks. The luminosity has to be corrected on a statistical basis using the z vertex distribution measured by the central tracker.

- **Dead-time correction**

When the trigger level 1 made a positive decision the H1 detector is no longer ready to detect new events. The duration of this dead-time depends on the higher level trigger decisions. If the event is kept, the data has to be read out completely. This takes typically 1-2 ms. At a typical L1 trigger rate of ~ 50 Hz this leads to a dead-time of 6-10%. It is calculated runwise.

- **High voltage correction**

During data taking some detector components may have problems. The information from these parts are missing. These events cannot be used for physics analysis. Therefore the high voltage information is included in the event data and can be used for the event selection. In this analysis the following subsystems must be fully operational:

- CJC, proportional chambers, forward tracker
- LAr calorimeter, Spacal
- instrumented iron
- ToF, VETO, lumi system
- forward muon system

The uncorrected integrated luminosity for the years 96 and 97 is 32.4 pb^{-1} . The resulting corrected luminosities are summarized in the following table.

Year	96	97	97
Run range	146416 - 171156	184258 - 193432	193433 - 200406
Subtrigger	34 \vee 87	34 \vee 87	15 \vee 34 \vee 87
Prescale	2.13 (s34) and 1.0 (s87)	1.29 (s34) and 1.0 (s87)	1.0 for all subtr.
\mathcal{L}	5.10 pb^{-1}	5.08 pb^{-1}	7.57 pb^{-1}

Table 4.7: Integrated luminosity after all corrections. Three run ranges are defined for different years or trigger setups. Also shown are the mean prescale factors.

The systematic error is determined in [16] and is 1.1%. The main contribution is due to differing acceptance and efficiencies for varying beam geometries (position and angle of incidence).

4.8 Picture of Typical Events

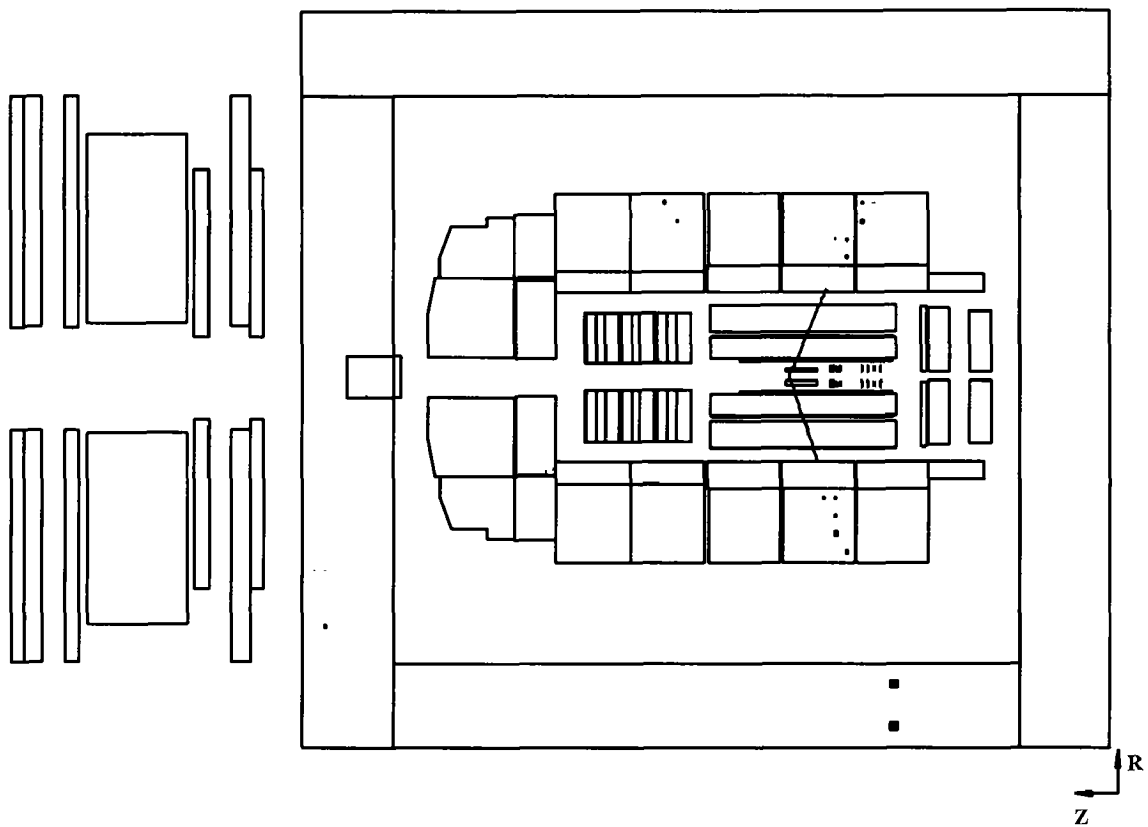


Figure 4.5: $r\phi$ view of a typical event with elastic muon pair production. Both muons show the signature of a minimal ionizing particle in the calorimeter. In addition, the lower muon leaves a track in the instrumented iron.

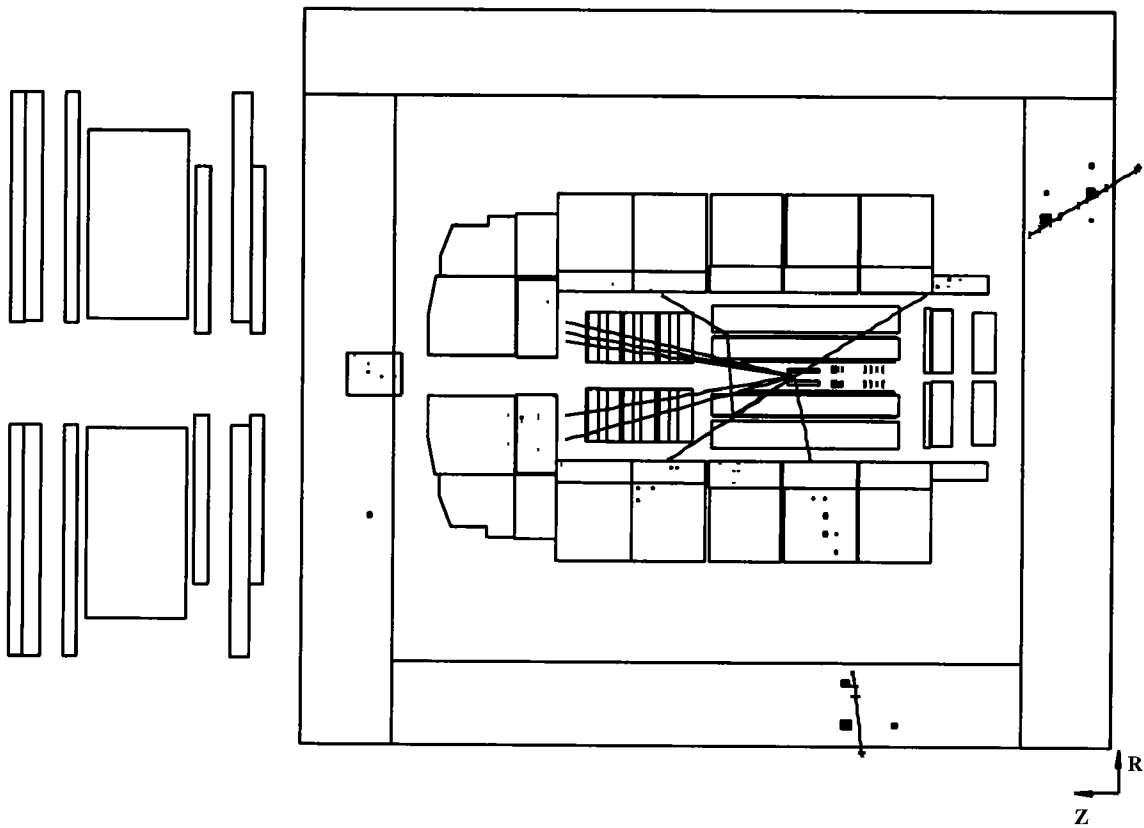


Figure 4.6: $r\Phi$ view of a typical event with proton dissociation. The muons are clearly separated from the jets.

Chapter 5

Measurement of the Cross Section

5.1 Background

The aim of the event selection cuts is (a) to define the event topology of interest, (b) to restrict the kinematics to a region, where the detector is well understood and (c) to separate the signal from the background. Points (a) and (b) have been explained extensively in chapter 4. In this section the rejection power of the cuts 6 and 7 are demonstrated and the remaining background is estimated.

Five different types of background processes are present.

1. Open heavy quark production with subsequent semileptonic decays. The muons are produced in the weak decays of the heavy quarks. E.g. for b quarks the two unlike sign muons originate either from the processes $b \rightarrow c\mu^-\bar{\nu}_\mu$ and $\bar{b} \rightarrow \bar{c}\mu^+\nu_\mu$, or from the sequential decay $b \rightarrow c\mu^-\bar{\nu}_\mu$, $c \rightarrow s\mu^+\nu_\mu$. In any case, the direction of flight of the muon is correlated with the jet thrust axis. This correlation has been studied in [12]. As can be seen there, the muon momentum perpendicular to the jet axis is relatively low. To reject these events, we demand two muons which are well separated in η and ϕ . This is demonstrated in figure 5.2.

The remaining events have been estimated with Monte Carlo simulation. The event generator AROMA 2.2 has been used. The number of events passing all selection cuts for the elastic and inelastic channels respectively are:

$$\begin{aligned} N_{b\bar{b}}^{el} &= 0.25 \\ N_{b\bar{b}}^{in} &= 16.9 \end{aligned}$$

The contribution from $c\bar{c}$ pairs is

$$\begin{aligned} N_{c\bar{c}}^{el} &< 0.05 \\ N_{c\bar{c}}^{in} &= 1.3 \end{aligned}$$

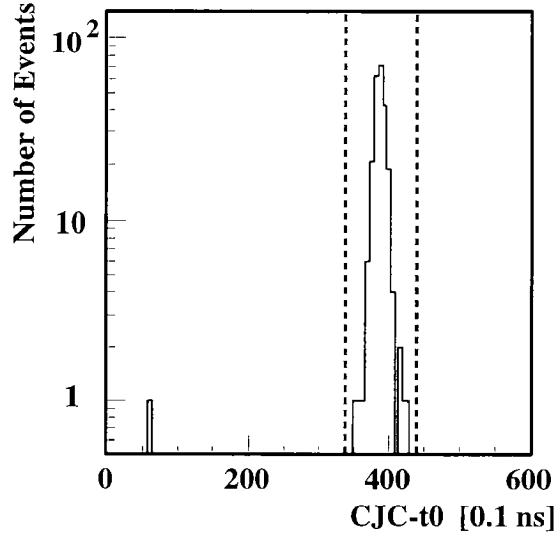


Figure 5.1: Distribution of the t_0 as measured by the CJC. All cuts are applied except the cut on t_0 . The interaction time window is defined by the two dashed lines.

2. Cosmic muons. A cosmic muon passing through the detector near the beam pipe is reconstructed as two muons coming from the center of the detector. The tracks are in a back to back configuration. The origin of the tracks is not correlated with the nominal interaction region and also the timing as measured by the central tracker CJC is arbitrary. All this can be used to cut on these events. It turns out, that the most efficient cut is the one on the opening angle. This can be seen in figure 5.3. In data a large peak can be seen at opening angles $> 165^\circ$.

The remaining cosmic events after applying all the selection cuts is estimated from data. The number of events outside the interaction time window of 5 ns around the nominal bunch crossing time has been extrapolated into this window. Only one event has been found outside (figure 5.1). This gives the estimation of

$$N_{cosmic}^{el} = 0.13$$

Since cosmic muons passing through the central tracker do not hit the very forward detectors, no event is expected in the inelastic channel.

3. Production of Υ mesons with subsequent decay into two muons. This has been studied in Monte Carlo. The p_T spectrum is too soft for the cuts. The expected number of events is < 0.1 . In the mass spectrum (section 5) no Υ signal has been found.
4. QED pair production of τ leptons. Tau leptons are decaying into muons with

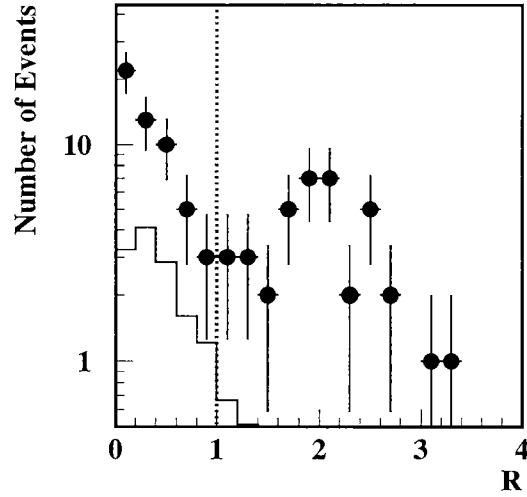


Figure 5.2: Distribution of R , the separation of the muons in the (η, ϕ) -plane. Points represent the data events with at least one track or energy cluster in addition to the muons. The histogram shows AROMA Monte Carlo simulating open $b\bar{b}$ production. The dotted line indicates the cut: entries on the left hand side are rejected. Only a subset of the data is shown.

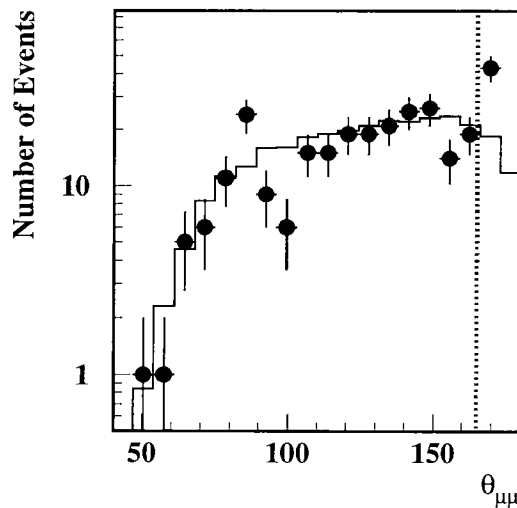


Figure 5.3: Distribution of the opening angle $\theta_{\mu\mu}$ of the two muons. Points represent data, the histogram shows LPAIR Monte Carlo simulation. The dotted line indicates the cut: entries on the right hand side are rejected. The data peak at the right end originates from cosmic muon events. Here a cut of $\theta_{\mu\mu} < 175^\circ$ has been made during the data pre-selection.

a branching ratio of 17.4%. Events, where both τ 's decay into muons, add to the background.

The effect has been investigated in Monte Carlo studies. A substantial part of the τ energy is carried away by the neutrinos. The decay muons mostly have a transverse momentum p_T below 1.8 GeV/c and thus fail the selection criteria. The remaining effect is 0.5% of the muon production cross section. Thus, the expected background from τ production is

$$\begin{aligned} N_{\tau\tau}^{el} &= 0.48 \\ N_{\tau\tau}^{in} &= 0.78 \end{aligned}$$

5. Fake muons. Hadrons, especially pions, may fake a muon in the detector. Thus, events with two well separated hadrons or one hadron and one muon could add to the background. This has been estimated from data. Events were selected, which passed all the selection cuts, with the exception that the two isolated tracks need not to be identified as muons. According to [29] to each track (not identified as a muon) there is assigned either a pion, a kaon or a proton. This particle assignment is based on the Lund string model for the hadronization as implemented in JETSET ([30]). The result is roughly 60% pions, 22% kaons and 18% protons. The number of background events then is estimated by multiplying with the probability $P_{\mu}^{\pi,K,p}$ for the corresponding hadron to fake a muon. These probabilities are well described in Monte Carlo simulation as pointed out in [29]. After applying the trigger efficiency one gets the following background estimation:

$$\begin{aligned} N_{fake}^{el} &= 0.50 \\ N_{fake}^{in} &= 7.35 \end{aligned}$$

Table 5.1 summarizes all contributions to the background for the elastic and inelastic channel.

5.2 Definition of Elastic and Inelastic Cross Section

The visible e^+p -cross section is determined by the formula

$$\sigma_{vis}^{el,in}(e^+p \rightarrow \mu^+\mu^-X) = \frac{N_{tot}^{el,in} - N_{background}^{el,in}}{\left(\sum_{run\ ranges} \epsilon_{sel,i} \cdot \epsilon_{trig,i} \cdot \mathcal{L}_i \right)} \quad (5.1)$$

where

	elastic	inelastic
Open $b\bar{b}$ production	0.25	16.9
Open $c\bar{c}$ production	<0.05	1.3
Cosmic muons	0.13	0.0
Υ production	<0.1	<0.1
τ pair production	0.48	0.78
Fake muons	0.50	7.35
Total	<1.51	26.4

Table 5.1: Summary of the contributions to the background to di-muon events in the elastic and inelastic channel respectively

- $N_{tot}^{el,in}$ is the total number of observed events passing all the cuts for elastic and inelastic events respectively
- $N_{background}^{el,in}$ is the expected number of background events in the respective channel
- $\epsilon_{sel,i}$ is the efficiency of the data selection in the run range i . It has the same value for both elastic and inelastic event selection.
- $\epsilon_{trig,i}$ is the trigger efficiency for the run range i . Since the distinction into trigger efficiency and trigger acceptance is not strict, this is not treated separately. Therefore, the product of the two is included in $\epsilon_{trig,i}$.
- \mathcal{L}_i is the integrated luminosity for the run range i

The efficiency for the data selection cuts 1 to 10 has been determined in chapter 4. Cuts 11 to 13 were introduced to distinguish elastic and inelastic events without further explanation. To make up for this and to determine its efficiency, we first have to define what we mean with an *elastic* or *inelastic* cross section.

Figure 5.4 shows a schematic view of an event. In the final state we see two systems denoted by X and Y . The system X consists of the scattered positron and the two created muons, while the system Y is the hadronic final state. One cannot distinguish between truly elastic events (with the system Y being a proton) and an event with proton dissociation, where the fragments escape the detector in the very forward direction. Therefore the term *elastic* in this analysis refers to all the events with no signal in the very forward direction (see section 4.4), that is the system Y is not seen in the forward muon device, the proton remnant tagger or in the LAr calorimeter. The complement is termed *inelastic*.

To compare this to the expectation one has to determine the acceptance for these cuts. In principle, this could be done similarly to the determination of the selection efficiency. However, a different approach is chosen here. The reason for this is the

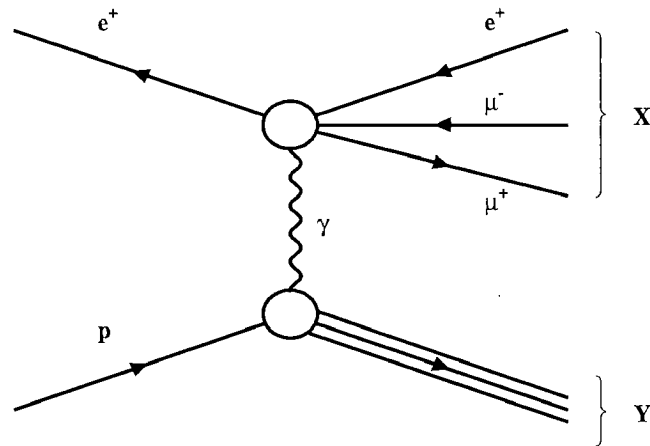


Figure 5.4: Schematics of an event in muon pair production. One observes two distinct final state systems. System X represents the leptonic final state, while system Y denotes the hadronic final state (which might contain leptons from quark decays).

following. In order to get a good estimation it is crucial that the simulation of the hadronic final state describes the data very well. This is true for the mean energy flow. However, in many events with small momentum transferred to the proton Q^2 only the edge of the jet may hit the detector and a detailed knowledge of the hadronic structure is needed. Since this is governed by long range physics, this is a weak point for all Monte Carlo generators and any dependency on this should be avoided. Therefore the following approach has been chosen.

Above $Q^2 = 1 \text{ (GeV/c)}^2$ the detection efficiency is taken from Monte Carlo simulation with LPAIR++. For $Q^2 < 1 \text{ (GeV/c)}^2$ the Monte Carlo generator is used to determine the global kinematic variables of the jet only. These are the mass of the hadronic final state M_Y and the square of the momentum transferred to the proton Q^2 . The detection efficiency as a function of these variables is known from analyzes in diffractive physics. In diffraction we are in the same situation, as there are two final state systems connected by the exchange of a color neutral object.

Such an analysis has been done by P. Thomson [19]. The detection efficiencies for the hadronic final states are shown in figures 5.5 and 5.6. The solid line indicates the fit to the data which has been used to determine the total detection efficiency. This efficiency corresponds to the acceptance $A_{inelastic}$ for the inelastic cross section since it gives the fraction of the total visible cross section with a signal from the system Y in the detector.

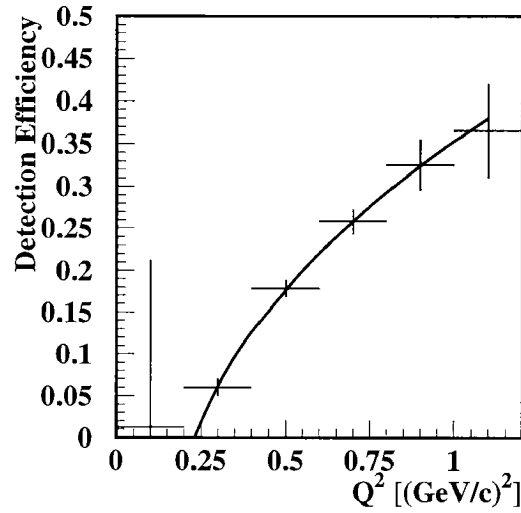


Figure 5.5: Detection efficiency for an elastically scattered proton as a function of Q^2 (see ref. [19]). The solid line shows the fit of a power function which is used in the Monte Carlo simulation.

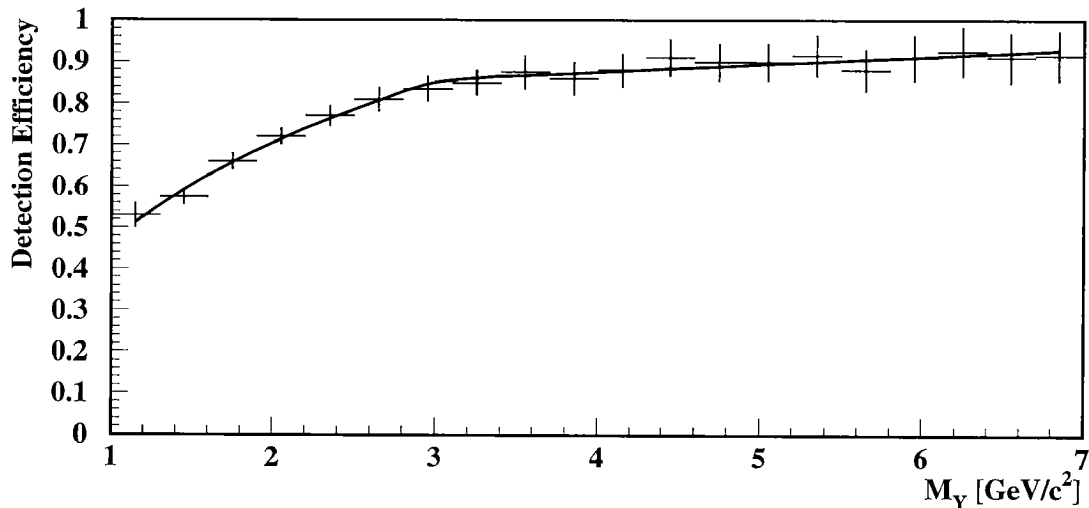


Figure 5.6: Detection efficiency for the system Y in proton dissociative processes as a function of the mass of the system Y . There is only a slight dependency on Q^2 which is neglected here (see ref. [19]). The solid line shows the fit which is used in the Monte Carlo simulation.

The acceptance did not change significantly during the years 96 and 97. The result is

$$A_{inelastic} = 36.2\%$$

The expected cross sections for the visible range are:

$$\begin{aligned}\sigma_{mc}^{el} &= (1 - A_{inelastic}) \cdot \sigma_{mc} = 29.7 \pm 1.8 \text{ pb} \\ \sigma_{mc}^{in} &= A_{inelastic} \cdot \sigma_{mc} = 16.8 \pm 1.0 \text{ pb}\end{aligned}$$

The error is explained in the next section.

5.3 Systematic Errors

In this section the systematic errors are determined. We begin with the error for the expectation.

5.3.1 Monte Carlo

1. According to chapter 2 there are three modes used to determine the visible cross section. The systematic error in each channel is estimated by the comparison of two independent generators, LPAIR++ and GRAPE. To do this comparison only two photon processes without ISR were used. The differences are:

elastic	0.5%
DIS	7%
resonance region	3%

Weighted with the corresponding cross sections this leads to an error of the total cross section of 2.2%.

2. In the DIS mode there is an additional uncertainty due to the parton density function (PDF) used. Using recent PDF's in LO or NLO, there is a difference of < 5.0%. For the total cross section, this leads to an error of 1.3%.
3. The generators used are leading order generators. Since it is pure QED, NLO corrections are of order $O(\alpha)$. It is estimated to < 1%.
4. The error of the detection efficiency for inelastic events $A_{inelastic}$ has two contributions. (a) the error in the differential detection efficiencies. This was determined in [19] and is indicated in the plots 5.5 and 5.6. (b) this has to be

folded with the relevant distributions (M_Y and Q^2 respectively) which depend on the relative portions of elastic and inelastic events. This error depends on the errors in item 1. The relative portions of inelastic events vary by 2.2%. The total error of $A_{inelastic}$ is 5.5%

We assume that all the above errors are uncorrelated. This gives a systematic error of the expected cross sections of 6.3% in both the elastic and the inelastic channel.

5.3.2 Data

1. The number of background events is estimated by a LO generator. NLO calculations show, that these contributions are large. The measured cross sections for open b and c production are even higher. Thus, the expected number of background events has been corrected by a factor 4.8 corresponding to the difference in measured and LO cross section. This assumes that the spectra have similar shapes, which cannot be checked, since there is no such event generator available. A conservative estimation of this error is 100% of the correction. This is 80% for the beauty and 20% for the charm.
2. The error of the track and muon reconstruction efficiency in the iron return yoke is estimated by a comparison of Monte Carlo simulation and data of the J/Ψ peak. This was explained in section 4.3. The difference of the simulation and data is 4%.
3. The reconstruction efficiency for muons in the calorimeter has been checked using iron muons (see section 4.3). The discrepancy between data and Monte Carlo simulation is used to estimate the error. It is 4%. An error in the track reconstruction efficiency adds to this. This is estimated in [17] and is 3%. This gives a total error for the muon reconstruction in the calorimeter of 5%.
4. The error of the trigger efficiency on level 1 has been determined from each trigger element separately by comparison with Monte Carlo simulation. The result is shown in table 4.3. On level 2/4 the influence of different reference subtriggers has been studied. The combined errors for the two trigger setups are

s34 \vee s87	9.1 %
s15 \vee s34 \vee s87	10.0 %

This gives a total error of the trigger efficiency of 9.5 %

5. The reconstruction of the invariant mass is imperfect. Events with a true mass which is higher than measured may wrongly fail the cuts. The opposite can

Monte Carlo	
Calculated cross section	2.2%
Parton density function	5.0%
Forward detection efficiency	5.5%
Total MC	6.1%
Data	
bb background	80%
$c\bar{c}$ background	20%
Muon reconstruction in the iron system	4.0%
Muon reconstruction in the calorimeter	5.0%
Trigger efficiency	9.5%
Mass reconstruction	1.3%
Integrated luminosity	1.1%
Total data	18% (inelastic), 11% (elastic)

Table 5.2: Summary of the systematic errors in Monte Carlo simulation and in data. Details can be found in the text.

happen as well. The two effects are not in balance. The net effect has been estimated in Monte Carlo studies. It is a 1.3% effect.

6. The error of the integrated luminosity is taken from [16] and is 1.1%

From the above we get an error for the number of events of 0.2% for elastic and 14% for inelastic events. The error for the muon *pair* reconstruction efficiency is 5.7%. Again assuming no correlation between the errors, the total systematic errors are 18% for the inelastic and 11% for the elastic cross section. The errors are summarized in table 5.2

5.4 Results

We are now ready to give the results. In the following table the efficiencies and luminosities needed in formula (5.1) are summarized.

Run range	146416 - 171156	184258 - 193432	193433 - 200406
Corrected luminosity	5.10 pb ⁻¹	5.08 pb ⁻¹	7.57 pb ⁻¹
Total trigger efficiency	42.4 %	60.5 %	79.7 %
Selection efficiency	48.7 %	47.4%	47.4%

The number of observed events is

$$N_{tot}^{el} = 144$$

$$N_{tot}^{in} = 134$$

The measured cross sections are:

$$\begin{aligned}\sigma_{meas}^{el}(e^+p \rightarrow \mu^+\mu^-X) &= (26.6 \pm 2.2 \pm 2.9) \text{ pb} \\ \sigma_{meas}^{in}(e^+p \rightarrow \mu^+\mu^-X) &= (20.2 \pm 2.4 \pm 3.6) \text{ pb}\end{aligned}$$

The first error is statistical and the second one is systematic.

Both cross sections are in good agreement with the expectation from the standard model. The deviation is less than one standard deviation in both cases.

5.5 Differential Distributions

In this section differential cross sections with respect to the invariant mass $M^{\mu\mu}$, the hadronic transverse momentum p_T^X and the missing transverse momentum p_T^{miss} are shown. This is done for the sum of elastic and inelastic events.

In figure 5.7 the mass spectra are shown. The efficiencies are determined for each bin separately. The statistics is such that the right most bin in the data corresponds to one measured event. Monte Carlo simulation and data are in good agreement. This is also true for the tail at high $M^{\mu\mu}$. The integrated cross section is

$$\int_{30 \text{ GeV}/c^2}^{\infty} \frac{d\sigma}{dM^{\mu\mu}} dM^{\mu\mu} = \begin{cases} 0.15 \pm 0.15 & \text{pb, Data} \\ 0.21 & \text{pb, MC} \end{cases}$$

If we look back to chapter 1 the distributions of special interest are the p_T^X and p_T^{miss} distributions. There, the single muon events show high values of these variables compared to the spectra from the background Monte Carlo simulations. The question arises, whether the description in the Monte Carlo simulation is correct. In figures 5.8 and 5.9 this is confirmed for the two photon generator LPAIR++. The measured spectra stop at $p_T^X = 12.1 \text{ GeV}/c$ and $p_T^{miss} = 8.5 \text{ GeV}/c$ respectively which is consistent with the prediction from Monte Carlo simulations as can be seen in the following

$$\begin{aligned}\int_{5 \text{ GeV}/c}^{\infty} \frac{d\sigma}{dp_T^X} dp_T^X &= \begin{cases} 1.44 \pm 0.55 & \text{pb, Data} \\ 0.66 & \text{pb, MC} \end{cases} \\ \int_{5 \text{ GeV}/c}^{\infty} \frac{d\sigma}{dp_T^{miss}} dp_T^{miss} &= \begin{cases} 0.44 \pm 0.29 & \text{pb, Data} \\ 0.61 & \text{pb, MC} \end{cases}\end{aligned}$$

The error contains the statistical error, the error of the selection and trigger efficiencies and the error due to the error in the energy measurement.

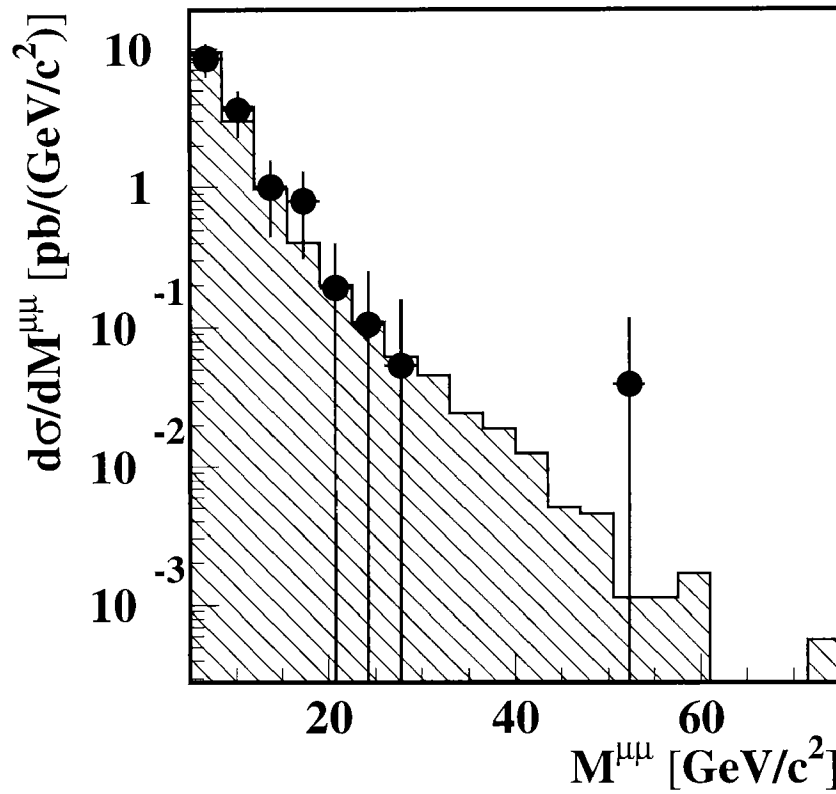


Figure 5.7: Differential cross section $d\sigma(ep \rightarrow \mu^+\mu^-X)/dM^{\mu\mu}$ for the sum of elastic and inelastic processes. The dashed histogram shows Monte Carlo simulation for the signal only (LPAIR++). Events with fake muons and heavy quark production are in the low mass region and are not visible on this logarithmic plot. Points represent data. The error bar is the sum of statistical and systematical errors. The right most bin in the data corresponds to one measured event.

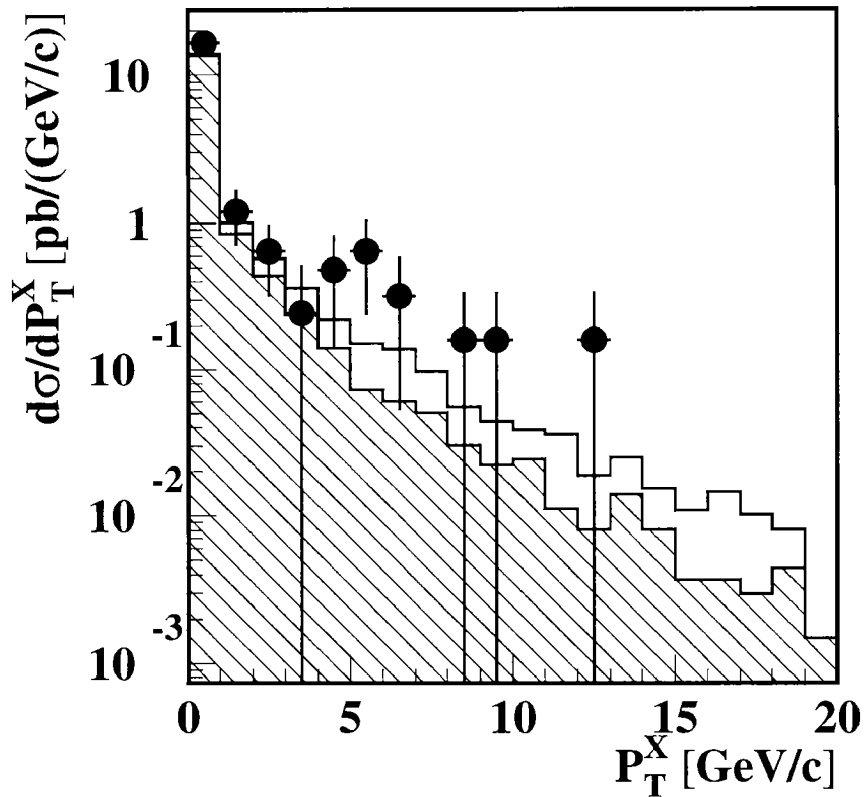


Figure 5.8: Differential cross section $d\sigma(ep \rightarrow \mu^+\mu^-X)/dp_T^X$ for inelastic events. The open histogram shows the expectation including events with fake muons and events from $b\bar{b}$ production Monte Carlo simulation (AROMA). The dashed histogram shows Monte Carlo simulation for the signal (LPAIR++), points represent data. The error bar is the sum of statistical and systematical error. The right most bin in the data corresponds to one measured event.

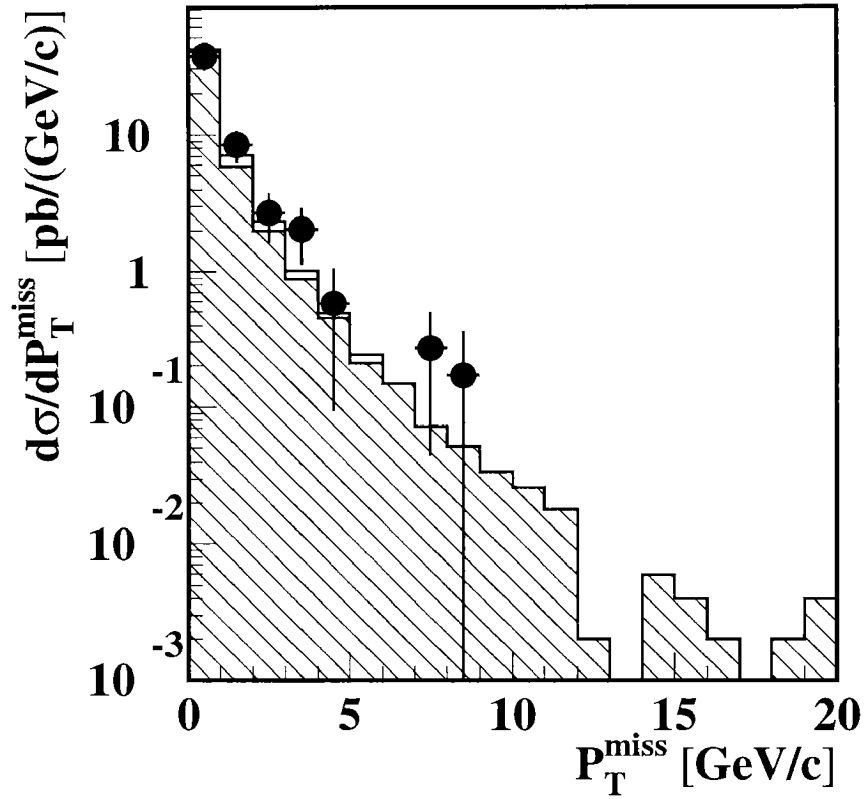


Figure 5.9: Differential cross section $d\sigma(ep \rightarrow \mu^+\mu^-X)/dp_T^{\text{miss}}$ for the sum of elastic and inelastic events. The open histogram shows the expectation including events with fake muons and events from $b\bar{b}$ production Monte Carlo simulation (AROMA). The dashed histogram shows Monte Carlo simulation for the signal (LPAIR++) only, points represent data. The error bar is the sum of statistical and systematical error. The right most bin in the data corresponds to one measured event.

5.6 Relaxed Muon Reconstruction Cuts

The reconstruction of muons has been described in chapter 4. The cuts have been chosen such that the reconstruction and trigger efficiencies are well described by Monte Carlo simulations of the detector. Back to the single muon events from chapter 1, we see that one of the 7 muon events does not fulfill the requirements for the muon reconstruction. The effect of relaxed requirements for muons are investigated in this section.

Looser cuts certainly cannot explain all the mismatch in the normalization seen in figures 1.2 and 1.3. However, the tails in the high momentum regime could be altered importantly. But this can be excluded as is shown in the following.

The new requirements for a track to be identified as a muon are:

1. The track must fulfill the quality requirements listed in chapter 4.1.
2. The polar angle must be in the range $20^\circ < \theta < 125^\circ$.
3. The isolation of the track in $\eta - \phi$ is at least 1.0
4. The total energy in the LAr calorimeter in a cylinder of radius 30 cm around the helix is less than 5 GeV
5. Within a distance in $\eta - \phi$ of 0.2 around the track, at least three strip electrodes of the instrumented iron system (see section 3.2.3) must have fired.

Some notes about these cuts:

The polar angle cut (2) is made to exclude the backward region, because there is too few material in front of the iron system. The misidentification rate would be too high.

The isolation (3) is required in order to reject jets with energy leakage through the LAr calorimeter.

Cut 5 is a very loose cut. The three strips can be part of the innermost muon box which is in front of the first iron layer. However, this is required for the muon event mentioned above.

The selection cuts are unaltered from section 4.4. A total of 35 events is added to the data sample with the 'old' reconstruction. In figure 5.10 the distributions of P_T^X and P_T^{miss} for the sum of elastic and inelastic events are plotted for both the 'old' and the 'relaxed' muon reconstruction cuts. The spectra do not differ significantly. The comparison with the simulation is shown in figure 5.11. The 'relaxed' cuts have been applied to both data and Monte Carlo simulation. The later has been normalized to the same total number of events. The shapes of the distributions agree within statistical errors.

With the additional muon reconstruction cuts it is harder to control efficiencies and the background from misidentified pions or kaons. At this point, this is not a problem, since this could only add additional events to the data sample. This even improves the significance of figures 5.10 and 5.11.

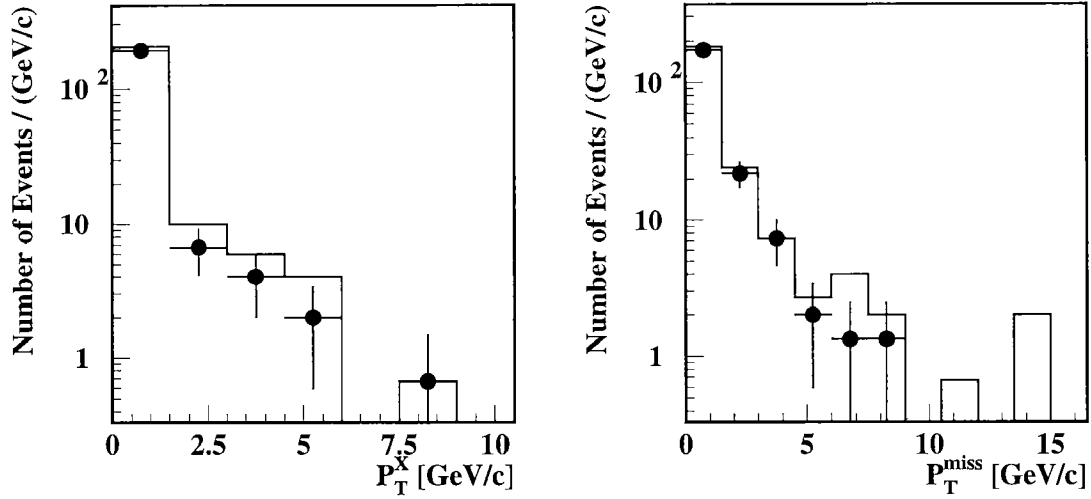


Figure 5.10: Differential distributions of P_T^X and P_T^{miss} . The points show the number of events with the muon cuts used in this analysis, while the histogram shows the number of events including muons reconstructed with the relaxed conditions described in the text. The two distributions do not differ significantly.

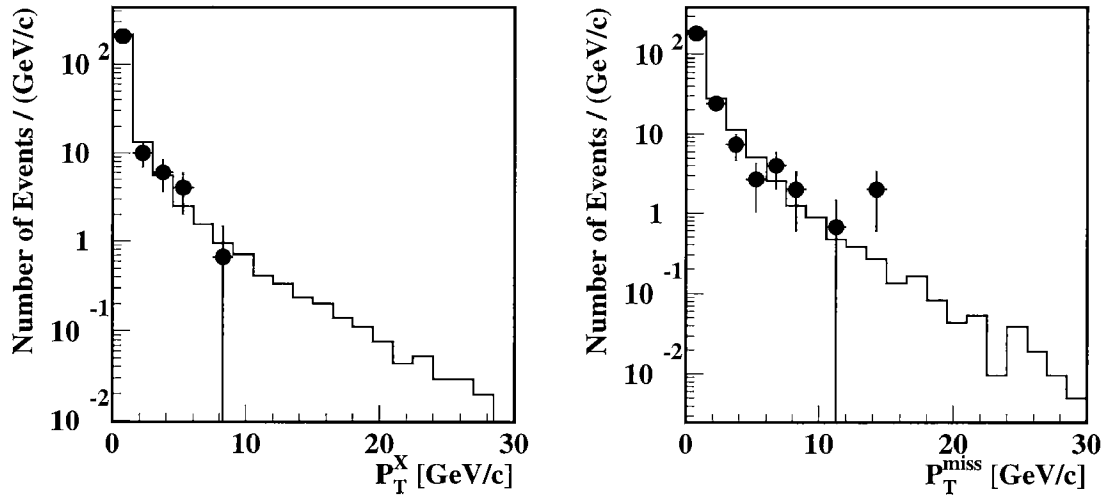


Figure 5.11: Differential distributions of P_T^X and P_T^{miss} . The points show the number of events including muons reconstructed with the relaxed conditions. The histogram shows the respective distribution from Monte Carlo simulation. The latter is normalized to the same total number of events.

Chapter 6

Multi Muon Events

So far, the event selection requested exactly two isolated muons. We will extend this here and look for multi muon events with two isolated muons. Since multi muon events are extremely rare compared to di-muon events, it is expected, that eventually appearing multi muon events contain one or more fake muons, that is hadrons misidentified as muons. This is investigated here.

We start with the data selection. The selection cuts are:

1. There must be at least 3 muons in the event
2. Three muons are in the polar angle range $20^\circ < \theta^\mu < 160^\circ$
3. Three muons have a transverse momentum $p_T^\mu > 1.8 \text{ GeV}/c$. For muons reconstructed in the calorimeter only, this cut is lowered to $2 \text{ GeV}/c < p^\mu < 4 \text{ GeV}/c$.
4. At least two of the muons are isolated in the rapidity - azimuth plane:
$$\Delta R = \sqrt{\Delta\eta^2 + \Delta\phi^2} > 0.8$$
5. The time as reconstructed in the jet chamber, must be within 5 ns around the nominal bunch crossing time.
6. The reconstructed z coordinate of the primary vertex must be in the range [-30 cm, +20 cm]
7. All relevant subdetector components must have been fully operational (see section 4.7 for details)
8. The event must have been triggered independently from the muon system.

The cuts 3 and 4 have been relaxed compared to the di-muon analysis. This is done, to gain more statistics. In the new kinematic region at low momenta, the reconstruction efficiencies are not known very well. However, we are not interested in a cross section here and thus don't need the efficiencies.

The data used were recorded in the year 1997. A total of 8 events have been found

with three muons each. Two typical events are shown at the end of this chapter. No events show the signature of 4 or more muons.

In order to estimate the number of events with fake muons a data set similar to the one above has been selected but with the cuts 1 to 4 replaced by:

1. There must be at least three tracks in the event
2. Three tracks must have polar angles in the range $20^\circ < \theta < 160^\circ$ and a momentum $p > 2$ GeV
3. At least two of the tracks from (2.) must be isolated:
 $\Delta R = \sqrt{\Delta\eta^2 + \Delta\phi^2} > 0.8$
4. There are at most two muons in the event

Tracks here means tracks which are not assigned to an electron/positron, because their fake probability can be omitted. The cuts 5 to 8 from above are unaltered. A total of 44118 events are selected. 219 of them have two reconstructed muons, 4853 have one reconstructed muon. The rest has no reconstructed muons. All subtriggers which are independent of the muon system are chosen here. This gives us the possibility for a very nice check for muon misidentification.

To all tracks, not reconstructed as a muon, a probability to fake either an iron muon or a calorimeter muon is assigned. As in chapter 5.1, these probabilities are taken from [29] for the instrumented iron and from [15] for calorimeter muons. For tracks with $p_T < 1.8$ GeV/c the fake probability in the iron is set to zero. Similarly the fake probability in the calorimeter for tracks with $p > 4$ GeV/c is set to zero.

From these numbers, a probability for an event to have 0, 1, 2, ..., n muons is calculated. Since the fake probability is typically of the order of 1%, most of the 'fake' events will be di-muon events with an additional fake muon, rather than events with two or three fake muons.

Figure 6.1 shows the number of expected and observed tri-muon events as a function of the number of iron muons. A total of 12.0 ± 6.2 events is expected compared to the 8 observed events. Also the shapes are in good agreement.

Figure 6.2 shows the expected and observed distributions in polar angle θ and sum of charges $\sum q_i$ of the muons for tri-muon events. They agree all within 2.2 standard deviations. The number of expected events with more than three muons is 0.26. No such event has been measured.

To conclude this, we can say, that the number of multi muon events and the distributions of θ and $\sum q_i$ is in good agreement with the expectation from events with fake muons.

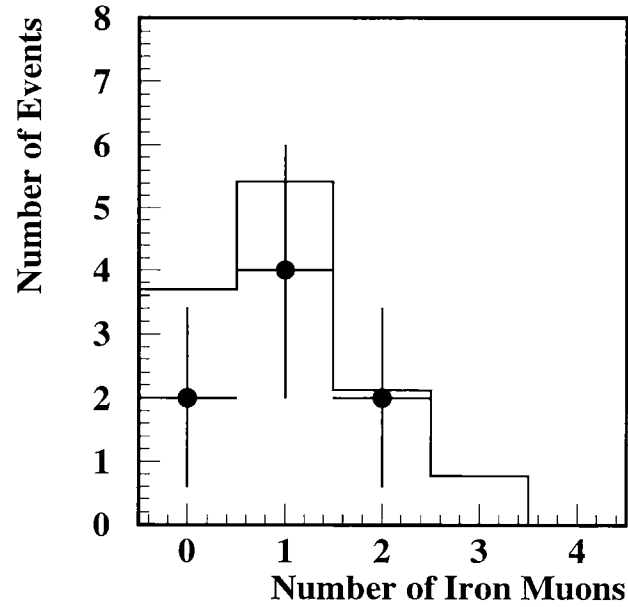


Figure 6.1: Number of observed (points) and expected (data) tri-muon events as a function of the number of iron muons. The error bar shows the statistical error.

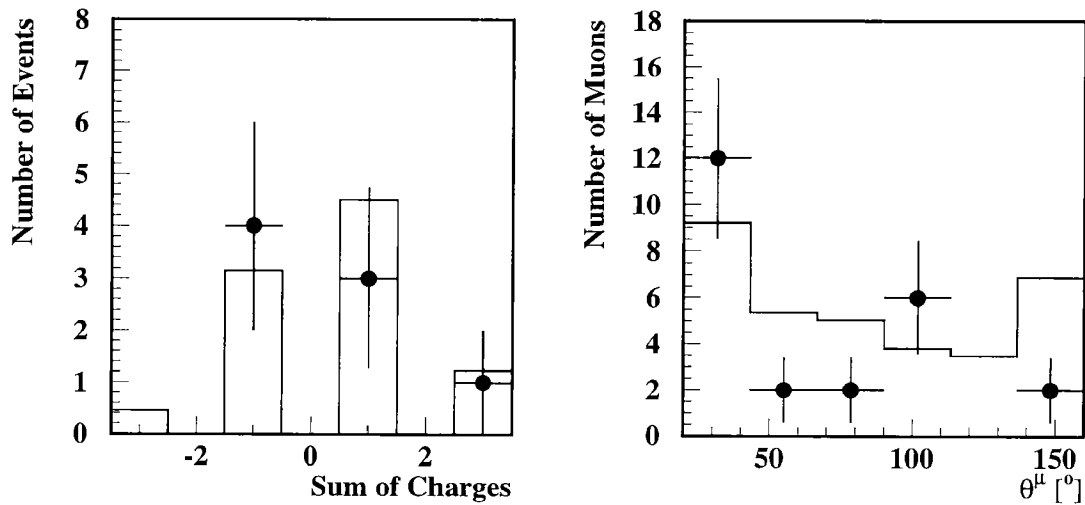
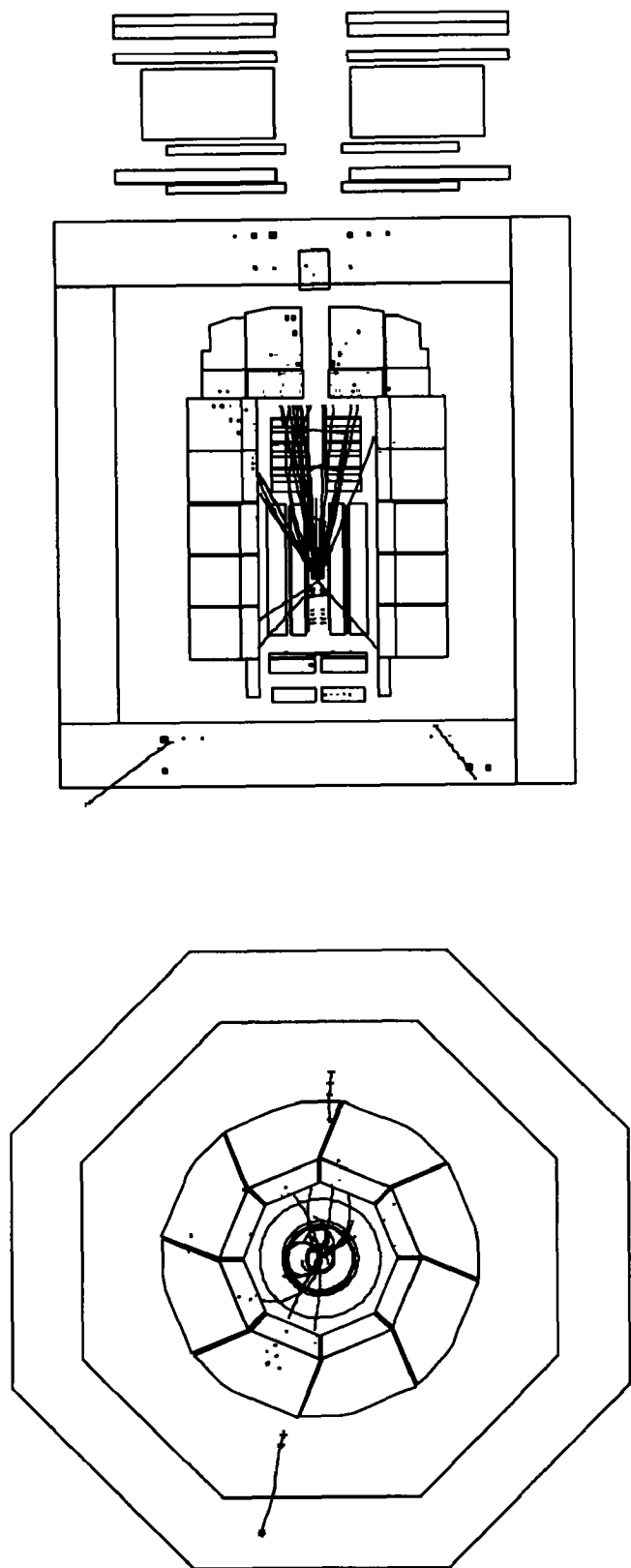
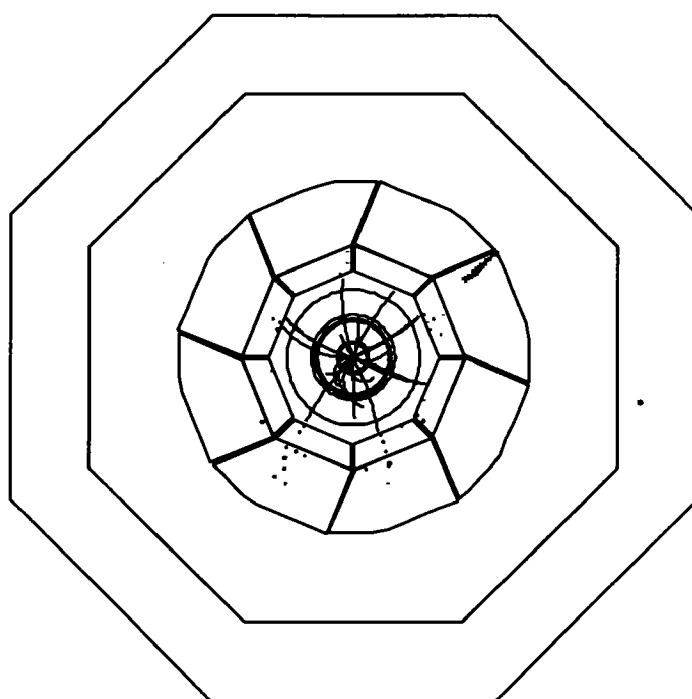
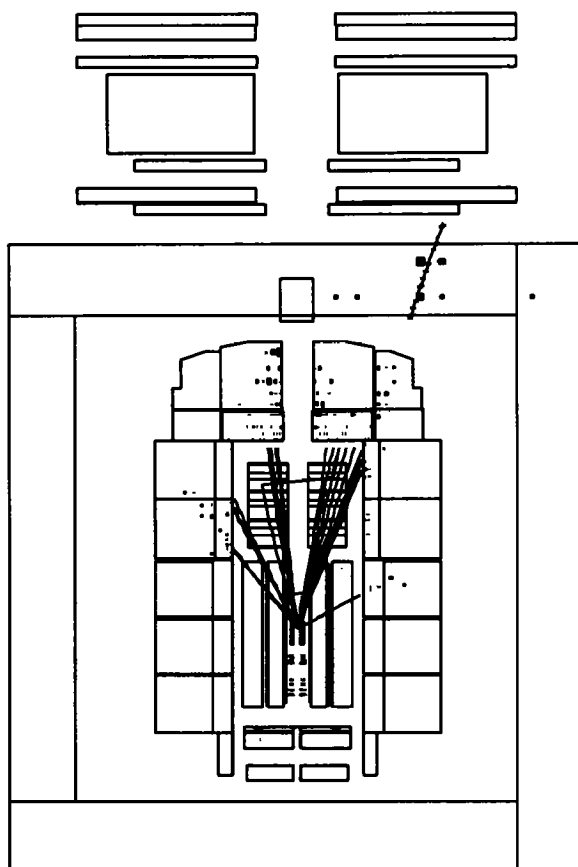


Figure 6.2: Observed (points) and expected (histogram) distributions in polar angle θ^μ and sum of charges $\sum q_i$ for tri-muon events. The error bar shows the statistical error.





Conclusions

The cross section for muon pair production with an invariant mass above 5 GeV/c² at HERA has been measured. The data taken during the years 96 and 97 has been used which corresponds to an integrated luminosity of 32.4 pb⁻¹. The corrected cross sections in the visible range ($M^{\mu\mu} \geq 5$ GeV/c², $20^\circ \leq \theta_{1,2}^\mu \leq 160^\circ$, $p_{T1,2}^\mu \geq 1.5$ GeV/c) are:

$$\begin{aligned}\sigma_{vis}^{el}(e^+p \rightarrow \mu^+\mu^-X) &= (26.6 \pm 2.2 \pm 2.9) \text{ pb} \\ \sigma_{vis}^{in}(e^+p \rightarrow \mu^+\mu^-X) &= (20.2 \pm 2.4 \pm 3.6) \text{ pb}\end{aligned}$$

The first error is statistical and the second is systematic.

The influence of processes other than the two photon graph has been investigated. It is only of the order of 0.5%. The expected cross sections from Monte Carlo simulations are

$$\begin{aligned}\sigma_{mc}^{el}(e^+p \rightarrow \mu^+\mu^-X) &= 29.7 \pm 1.8 \text{ pb} \\ \sigma_{mc}^{in}(e^+p \rightarrow \mu^+\mu^-X) &= 16.8 \pm 1.0 \text{ pb}\end{aligned}$$

which is in good agreement with the data.

The spectra P_T^X and P_T^{miss} are in fairly good agreement with the expectation. No events with two muons and large P_T^{miss} are observed. The upper limit for the production cross section of two muons with $P_T^{miss} > 10$ GeV/c is 0.45 pb at 90 % CL.

No candidate for an event $ep \rightarrow Z^0 X$ has been found. This gives an upper limit for the Z^0 production cross section ¹ of

$$\begin{aligned}\sigma(ep \rightarrow Z^0 X) &< 2.44 \cdot \left(\sum_{run\ ranges} \epsilon_{sel,i} \cdot \epsilon_{trig,i} \cdot \mathcal{L}_i \cdot BR(Z^0 \rightarrow \mu\mu) \right)^{-1} \\ &= 13.1 \text{ pb, at 90\% CL.},\end{aligned}$$

where $BR(Z^0 \rightarrow \mu\mu)$ is the branching ratio for the Z^0 to decay into two muons or two taus which decay into muons.

¹see Particle Data Group, C. Caso, *et al.*, Eur. Phys. J. C3, 1998, p. 177

Multimuon events have been observed. Since production cross sections for multi muon events are very small, the observed events are expected to be events with fake muons. This could be confirmed on a statistical basis. 8 events have been observed with an expectation of 12.0 ± 6.2 events.

The error for the expectation of single isolated muon events from two photon physics (LPAIR) in table 1.1 could be lowered substantially. This error was mainly due to uncertainties on generator level, since there was not enough statistics to test it.

As a final remark, one can say, that in the kinematic range defined above, the measurement of muons in H1 is well understood. The di-muon physics is in good agreement with standard model physics. No hint for physics beyond the standard model has been found. The error of the background expectation for isolated single muon production could be lowered, which makes the discrepancy even more significant.

Bibliography

- [1] Kleiss, R., Stirling, W.J., *Spinor Techniques for Calculating $p\bar{p} \rightarrow W^\pm / Z^0 + \text{Jets}$* , Nucl. Phys. B262 (1985) 235-262
- [2] Hilgart, J., Kleiss, R., *An electroweak Monte Carlo for four-fermion production*, Comp. Phys. Comm. 75 (1993) 191
- [3] CDF Collaboration, *Searches for New Physics in Diphoton Events in $p\bar{p}$ collisions at $\sqrt{s}=1.8$ TeV*, Phys. Rev. D59 092002 (1999)
- [4] H1 Collaboration, *Observations of Events with an Isolated High Energy Lepton and Missing Transverse Momentum at HERA*, DESY-98-063 / Eur. Phys. J. C5 (1998) 575-584
- [5] H1 Collaboration, *A Search for Excited Fermions at HERA*, to be published.
- [6] H1 Collaboration, *A Search for Squarks of Rp-Violating SUSY at HERA*, Z. Phys. C71 (1996) 211
- [7] H1 Collaboration, *The H1 Detector at HERA*, Nucl. Instr. and Meth. A386 (1997) 310-396
- [8] Pitzl, D. et al. *The H1 Silicon Vertex Detector*, hep-ex/0002044.
- [9] Bürger, J. et al. *The Central Jet Chamber of the H1 Experiment*, Nucl Instr. and Meth. A279 (1989) 217
- [10] Andrieu, B. et al. *The H1 Liquid Argon Calorimeter System*, Nucl. Instr. and Meth. A336 (1993) 460
- [11] Müller, D. (1998), *A Measurement of the Gluon Density in the Proton Based on Charm Production at HERA*, Ph. D. thesis University of Zürich
- [12] Langenegger, U. (1998), *A Measurement of the Beauty and Charm Production Cross Sections at the ep Collider HERA*, Ph. D. thesis ETH Zürich, No. 12676
- [13] Kleinwort, C., Krüger, U. (1992), *Iron muon track reconstruction*, H1-software note 92-035

- [14] Schiek, S. (1996), *Untersuchung der inelastischen Photoproduktion von J/Ψ -Mesonen im H1-Detektor bei HERA*, Ph. D. thesis University of Hamburg
- [15] Schmidt, G., (1997), *Untersuchung der diffraktiven Photoproduktion von J/Ψ -Mesonen im H1 Detektor bei HERA*, Ph. D. thesis University of Hamburg
- [16] H1 Collaboration (1996), *Luminosity Measurement in the H1 Experiment at HERA*, XXVII ICHEP, Warsaw.
- [17] Erdmann, W. (1996), *Untersuchung der Photoproduktion von D^* -Mesonen am ep-Speicherring HERA*, Ph. D. thesis ETH Zürich, No. 11441
- [18] Negri et al. (1996), *A Minimal Comprehensive Set of Muon Background Topological Finders for high p_T Physics Analysis*, H1-Note H1-10/96-498
- [19] Thomson, P. (1999), *Open Charm Production in Inclusive and Diffractive Deep-Inelastic Scattering at HERA*, Ph. D. thesis University of Birmingham
- [20] Merkel, P. (1996), *Untersuchung von Myonpaaren mit hoher invarianter Masse im H1-Detektor bei HERA*, diploma thesis University of Hamburg
- [21] Arteaga-Romero, Carimalo, Kessler, *High p_T lepton pair production at ep-colliders: comparison between various production mechanisms*, Z. Phys. C52 (1991) 289-295
- [22] Vermaseren, J.A.M. *Two-Photon Processes at very high Energies*, Nucl. Phys. B229 (1982) 347-371
- [23] Dünger, O. (1994), *Untersuchung der Myonpaar-Erzeugung durch Photon-Photon-Kollision am e-p-Speicherring*, Ph. D. thesis University of Hamburg
- [24] Rosenbluth, M.N. *High Energy Elastic Scattering of Electrons on Protons*, Phys. Rev. 79 (1950) 615
- [25] Borkowski, F. et al., *Electromagnetic Form Factors of the Proton at low Momentum Transfer (II)*, Nucl. Phys. B93 (1975) 461-478
- [26] Suri, A. Yennie, D.R. *The Space-Time Phenomenology of Photon Absorption and Inelastic Electron Scattering*, Annals of Physics 72 (1972) 243-292
- [27] Brasse F.W. et al *Parameterization of the q^2 Dependence of γp Total Cross Section in the Resonance Region*, Nucl. Phys. B110 (1976) 413
- [28] CTEQ Collaboration: MSUHEP-60426, CTEQ-605
- [29] Langenegger, U. and Tsipolitis, G. *On Muon Identification in the Barrel of the H1 Detector*, H1-Note H1-04/98-542
- [30] Sjöstrand, T., Bengtsson, M., Comp. Phys. Commun. 43 (1987) 367

- [31] Abe, T. et al., *GRAPE-Dilepton. A Generator for Dilepton Production in ep Collisions*, Proceedings of the workshop 'Monte Carlo Generators for HERA Physics' 1998/99, DESY-Proc-1999-02

Acknowledgements

It has been a great pleasure to have the opportunity to work in such a large experiment like H1. I would like to express my gratitude to Ralph A. Eichler who made this possible. Discussions with him were very productive, since he always comes straight to the point.

I would like to thank Prof. André Rubbia for readily accepting to be co-examiner. His suggestions improved this theses considerably.

A special thank goes to Christoph Grab who introduced me into H1 software and physics analysis. He is gone far out of his way to help me with any kind of problems.

I am grateful to Urs Langenegger for helping to find my way in the collaboration and for introducing me into the trigger hardware. His kindness added much to make my sojourns in Hamburg as pleasant as they have been.

A thank goes to all members of the Zürich group for important discussions and for having good times also in the spare time. I would like to mention especially Johannes Gassner, Stefan Lüders, Michael Hilgers, Stefano Passaggio, Hubert Niggli and Yorgos Tsipolitis.

Last but not least I want to sincerely thank my beloved girlfriend Cornelia, my parents and my sister for their patience and moral support. They always kept me going.

Curriculum vitae

Name Hans-Christian Kästli
Born November 14th 1970, in Schiers GR
Citizenship Luzern (GR), Switzerland

Education

1977 - 1983 Primary School, Pany
1983 - 1985 Secondary School, Küblis
1985 - 1990 High School, Evangelische Mittelschule, Schiers
1990 Matura, type C
1990 - 1997 Study of Physics at the Swiss Federal Institute of
Technology (ETH) in Zürich
1997 Diploma in Theoretical Physics at the ETH Zürich
Title of thesis: "One loop QCD corrections to the
 $q\bar{q} \rightarrow l\bar{\nu}u\bar{d}$ amplitude"
1997 - 2000 Graduate education in experimental particle physics
at the ETH Zürich.